

500
C23
02/13

Report No.
UCB/SEMM-2002/13

**STRUCTURAL ENGINEERING,
MECHANICS AND MATERIALS**

**Perfectly Matched Layers for
Transient Elastodynamics of
Unbounded Domains**

by

Ushnish Basu

and

Anil K. Chopra

Copyright © 2002

December 2002

**Department of Civil and Environmental Engineering
University of California, Berkeley
Berkeley, California**

Perfectly Matched Layers for Transient Elastodynamics of Unbounded Domains

by

Ushnish Basu

and

Anil K. Chopra

Research conducted under
Contract/grant no. DACW39-98-K-0038
from the Waterways Experiment Station,
U.S. Army Corps of Engineers

Copyright © 2002

Report No. UCB/SEMM-2002/13
Structural Engineering, Mechanics and Materials
Department of Civil and Environmental Engineering
University of California, Berkeley

December 2002

Perfectly matched layers for transient elastodynamics of unbounded domains

Ushnish Basu and Anil K. Chopra^{*,†}

Department of Civil and Environmental Engineering, University of California, Berkeley, CA 94720, U.S.A.

SUMMARY

One approach to the numerical solution of a wave equation on an unbounded domain uses a bounded domain surrounded by an absorbing boundary or layer that absorbs waves propagating outwards from the bounded domain. A perfectly matched layer (PML) is an unphysical absorbing layer model for linear wave equations that absorbs, almost perfectly, outgoing waves of all non-tangential angles-of-incidence and of all non-zero frequencies. In an earlier work, the authors presented, *inter alia*, time-harmonic governing equations of PMLs for anti-plane and for plane-strain motion of (visco-)elastic media. This paper presents a) corresponding time-domain, displacement-based governing equations of these PMLs, and b) displacement-based finite-element implementations of these equations, suitable for direct transient analysis. The finite-element implementation of the anti-plane PML is found to be symmetric, whereas that of the plane-strain PML is not. Numerical results are presented for the anti-plane motion of a semi-infinite layer on a rigid base, and for the classical soil-structure interaction problems of a rigid strip-footing on a i) half-plane, ii) layer on a half-plane, and iii) layer on a rigid base. These results demonstrate the high accuracy achievable by PML models even with small bounded domains.

KEY WORDS: Perfectly matched layers (PML); Absorbing boundary; Scalar wave equation; Elastic waves; Transient analysis; Finite elements (FE)

*Correspondence to: Anil K. Chopra, Department of Civil and Environmental Engineering, 707 Davis Hall, University of California, Berkeley, CA 94720, U.S.A.

†E-mail: chopra@ce.berkeley.edu

Contract/grant sponsor: Waterways Experiment Station, U.S. Army Corps of Engineers; Contract/grant number: DACW39-98-K-0038.

CONTENTS

List of Figures	iii
1 Introduction	1
2 Anti-plane motion	3
2.1 Elastic medium	3
2.2 Perfectly matched layer	3
2.3 Time-domain equations for the PML	4
2.4 Finite element implementation	7
2.5 Numerical results	10
2.6 Caveat emptor	13
3 Plane-strain motion	16
3.1 Elastic medium	16
3.2 Perfectly matched layer	16
3.3 Time-domain equations for the PML	18
3.4 Finite element implementation	19
3.5 Numerical results	21
4 Conclusions	36
Appendix A	37
References	38
Notation	41

LIST OF FIGURES

1	A PML adjacent to a “bounded” (truncated) domain	5
2	Semi-infinite layer on fixed base, and a PML model	10
3	Input displacement and its Fourier transform	11
4	Nodal reactions of semi-infinite layer on fixed base	12
5	Dynamic stiffness of elastic semi-infinite layer on fixed base	14
6	Dynamic stiffness of visco-elastic semi-infinite layer on fixed base	15
7	Rigid strip on half-plane, and a PML model	23
8	Reactions of rigid strip on half-plane	24
9	Dynamic flexibility of rigid strip on elastic half-plane	26
10	Dynamic flexibility of rigid strip on visco-elastic half-plane	27
11	Rigid strip on layer on half-plane, and a PML model	28
12	Reactions of rigid strip on layer on half-plane	29
13	Dynamic flexibility of rigid strip on elastic layer on half-plane	30
14	Dynamic flexibility of rigid strip on visco-elastic layer on half-plane	31
15	Rigid strip on layer on rigid base, and a PML model	32
16	Reactions of rigid strip on layer on rigid base	33
17	Dynamic flexibility of rigid strip on elastic layer on rigid base	34
18	Dynamic flexibility of rigid strip on visco-elastic layer on rigid base	35

1. INTRODUCTION

Solution of the elastodynamic wave equation over an unbounded domain finds applications in soil-structure interaction analysis [1] and in the simulation of earthquake ground motion [2]. The need for realistic models often compels a numerical solution using a bounded domain, along with an artificial absorbing boundary or layer that simulates the unbounded domain beyond. Of particular importance are absorbing boundaries that allow transient analysis, facilitating incorporation of non-linearity within the bounded domain.

Typical approximate absorbing boundaries [3–6], although local and cheaply computed, may require large bounded domains for satisfactory accuracy, since typically they absorb incident waves well only over a small range of angles-of-incidence. For satisfactory performance, approximate absorbing layer models [7,8] require careful formulation and implementation to eliminate spurious reflections from the interface to the layer. The superposition boundary [9] is cumbersome and expensive to implement, and infinite elements [10,11] typically require problem-dependent assumptions on the wave motion. Rigorous absorbing boundaries are typically formulated in the frequency domain [12–14]; corresponding time-domain formulations [15–17] may be computationally expensive and may not be applicable to all problems of interest.

The difficulty in obtaining a sufficiently accurate, yet not-too-expensive model of the unbounded domain directly in the time domain has led to the use of traditional frequency-domain models towards time-domain analysis. One such method uses hybrid frequency–time-domain analysis [1,18], iterating between the frequency and time domains in order to account for nonlinearity in the bounded domain; this computationally demanding method requires careful implementation to ensure stability. Another approach replaces the nonlinear system by an equivalent linear system [19] whose stiffness and damping values are compatible with the effective strain amplitudes in the system. A third approach [20–22] approximates the frequency-domain DtN map of a system by a rational function and uses this approximation to obtain a time-domain system that is temporally local. Although this approach is conceptually attractive, computation of an accurate rational-function approximation may be expensive.

A perfectly matched layer (PML) is an absorbing layer model for linear wave equations that absorbs, almost perfectly, propagating waves of all non-tangential angles-of-incidence and of all non-zero frequencies. First introduced in the context of electromagnetic waves [23, 24], the concept of a PML has been applied to other linear wave equations [25–27], including the elastodynamic wave equation [28,29]. In a recent work [30], the authors have developed the concept of a PML in the context of frequency-domain elastodynamics, utilising insights obtained from PMLs in electromagnetics, and illustrated it using the one-dimensional rod on elastic foundation and the anti-plane motion of a two-dimensional continuum, governed by the Helmholtz equation. Extending the PML concept to the displacement formulation of plane-strain and three-dimensional motion, they have also presented a novel displacement-based, symmetric finite-element implementation of such a PML.

The objective of this paper is to present a) time-domain, displacement-based, equations

of the PMLs for anti-plane and for plane-strain motion of a (visco-)elastic medium, and b) displacement-based finite-element (FE) implementations of these equations. The frequency-domain PML equations from Ref. 30 are first transformed into the time domain by a special choice of the coordinate-stretching functions, and then these time-domain equations are implemented numerically by a straightforward finite-element approach. Time-domain numerical results are presented for the anti-plane motion of a semi-infinite layer on rigid base and for the classical soil-structure interaction problems of a rigid strip-footing on a i) half-plane, ii) layer on a half-plane, and iii) layer on a rigid base. Additionally, the adequacy of the special choice of the stretching functions towards attenuating evanescent waves is investigated through numerical results in the frequency domain. This paper presents only a brief explanation of the concept of a PML; a detailed development, and the derivation of the frequency-domain equations are presented in Ref. 30.

Tensorial and indicial notation will be used interchangeably in this paper; the summation convention will be assumed unless an explicit summation is used or it is mentioned otherwise. An italic boldface symbol will represent a vector, e.g., \mathbf{x} , an upright boldface symbol will represent a tensor or its matrix in a particular orthonormal basis, e.g., \mathbf{D} , and a sans-serif boldface symbol will represent a fourth-order tensor, e.g., \mathbf{C} ; the corresponding lightface symbols with Roman subscripts will denote components of the tensor, matrix or vector. An overbar over a symbol, e.g., $\bar{\mathbf{u}}$, denotes a time-harmonic quantity; such distinguishing notation was not employed in Ref. 30 because the entire analysis was in the frequency domain.

2. ANTI-PLANE MOTION

2.1. Elastic medium

Consider a two-dimensional homogeneous isotropic elastic continuum undergoing only anti-plane displacements in the absence of body forces. For such motion, if the x_3 -direction is taken to point out of the plane, only the 31- and 32-components of the three-dimensional stress and strain tensors are non-zero. The displacements $u(\mathbf{x}, t)$ are governed by the following equations ($i \in \{1, 2\}$):

$$\sum_i \frac{\partial \sigma_i}{\partial x_i} = \rho \ddot{u}, \quad (1a)$$

$$\sigma_i = \mu \varepsilon_i, \quad (1b)$$

$$\varepsilon_i = \frac{\partial u}{\partial x_i} \quad (1c)$$

where μ is the shear modulus of the medium and ρ its mass density; σ_i and ε_i represent the 3*i*-components of the stress and strain tensors.

On an unbounded domain, Eq. (1) admits plane shear wave solutions [31] of the form

$$u(\mathbf{x}, t) = \exp[-ik_s \mathbf{x} \cdot \mathbf{p}] \exp(i\omega t) \quad (2)$$

where $k_s = \omega/c_s$ is the wavenumber, with wave speed $c_s = \sqrt{\mu/\rho}$, and \mathbf{p} is a unit vector denoting the propagation direction.

2.2. Perfectly matched layer

The discussion of PML presented here is a synopsis of the corresponding development in Ref. 30. The summation convention is abandoned in this section.

Consider a wave of the form in Eq. (2) propagating in an unbounded elastic domain, the x_1 - x_2 plane, governed by Eq. (1). The objective of defining a perfectly matched layer (PML) is to simulate such wave propagation by using a corresponding bounded domain.

The governing equations of a PML are most naturally defined in the frequency domain, through frequency-dependent, complex-valued coordinate stretching. Assuming harmonic time-dependence of the displacement, stress and strain, e.g., $u(\mathbf{x}, t) = \bar{u}(\mathbf{x}) \exp(i\omega t)$, with ω the frequency of excitation, the governing equations of the PML for anti-plane motion are

$$\sum_i \frac{1}{\lambda_i(x_i)} \frac{\partial \bar{\sigma}_i}{\partial x_i} = -\omega^2 \rho \bar{u}, \quad (3a)$$

$$\bar{\sigma}_i = \mu \bar{\varepsilon}_i, \quad (3b)$$

$$\bar{\varepsilon}_i = \frac{1}{\lambda_i(x_i)} \frac{\partial \bar{u}}{\partial x_i} \quad (3c)$$

where λ_i are nowhere-zero, continuous, complex-valued coordinate stretching functions.

If the stretching functions are chosen as

$$\lambda_i(x_i) := 1 - i \frac{f_i(x_i)}{k_s} \quad (4)$$

in terms of real-valued, continuous attenuation functions f_i , then Eq. (3) admits solutions of the form

$$\bar{u}(\mathbf{x}, t) = \exp \left[- \sum_i F_i(x_i) p_i \right] \exp [-i k_s \mathbf{x} \cdot \mathbf{p}] \quad (5)$$

where

$$F_i(x_i) := \int_0^{x_i} f_i(\xi) d\xi \quad (6)$$

Thus, if $F_i(x_i) > 0$ and $p_i > 0$, then the wave solution admitted in the PML medium is of the form of the elastic-medium solution [Eq. (2)], but with an imposed spatial attenuation. This attenuation is of the form $\exp[-F_i(x_i)p_i]$ in the x_i -direction, and is independent of the frequency if p_i is.

Consider replacing the x_1 - x_2 plane by $\Omega_{\text{BD}} \cup \Omega_{\text{PM}}$, as shown in Fig. 1, where Ω_{BD} is a ‘‘bounded’’ (truncated) domain, governed by Eq. (1), and Ω_{PM} is a PML, governed by Eq. (3), with λ_1 of the form in Eq. (4), satisfying $f_1(0) = 0$, and $\lambda_2 \equiv 1$. The medium in Ω_{BD} being a special PML medium [$\lambda_i(x_i) \equiv 1$], the matching of stretching functions at the Ω_{BD} - Ω_{PM} interface makes the PML ‘‘perfectly matched’’ to Ω_{BD} : waves travelling outward from the bounded domain are absorbed into the PML without any reflection from the Ω_{BD} - Ω_{PM} interface. An outgoing wave entering the PML is attenuated in the layer and then reflected back from the fixed end towards the bounded domain. If the incident wave has unit amplitude, then the amplitude $|R|$ of the reflected wave as it exits the PML is given by

$$|R| = \exp [-2F_1(L_P) \cos \theta] \quad (7)$$

This reflected-wave amplitude is controlled by the choice of the attenuation function and the depth of the layer, and can be made arbitrarily small for non-tangentially incident waves. Because such outgoing waves in such a system will be only minimally reflected back towards the interface, this bounded-domain-PML system is an appropriate model for the unbounded x_1 - x_2 plane.

2.3. Time-domain equations for the PML

Consider two rectangular Cartesian coordinate systems for the plane as follows: 1) an $\{x_i\}$ system, with respect to an orthonormal basis $\{\mathbf{e}_i\}$, and 2) an $\{x'_i\}$ system, with respect to another orthonormal basis $\{\mathbf{e}'_i\}$, with the two bases related by the rotation-of-basis matrix \mathbf{Q} , with components $Q_{ij} := \mathbf{e}_i \cdot \mathbf{e}'_j$. Equation (3) can be re-written in terms of the coordinates x'_i by replacing x_i by x'_i throughout, representing a medium wherein waves are attenuated in

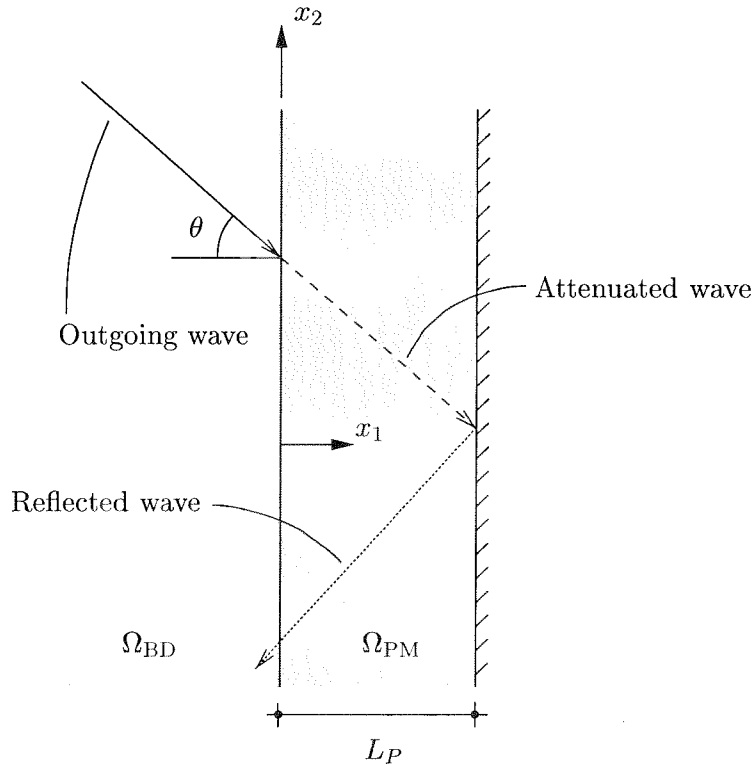


Figure 1. A PML adjacent to a “bounded” (truncated) domain attenuates and reflects back an outgoing plane wave.

the \mathbf{e}'_1 and \mathbf{e}'_2 directions, rather than in the \mathbf{e}_1 and \mathbf{e}_2 directions as in Eq. (3). This resultant equation can be transformed to the basis $\{\mathbf{e}_i\}$ to obtain [30]

$$\nabla \cdot (\tilde{\Lambda} \bar{\boldsymbol{\sigma}}) = -\omega^2 \rho [\lambda_1(x'_1) \lambda_2(x'_2)] \bar{u}, \quad (8a)$$

$$\bar{\boldsymbol{\sigma}} = \mu(1 + 2ia_0\zeta) \bar{\boldsymbol{\varepsilon}}, \quad (8b)$$

$$\bar{\boldsymbol{\varepsilon}} = \Lambda (\nabla \bar{u}) \quad (8c)$$

where

$$\bar{\boldsymbol{\sigma}} := \begin{Bmatrix} \bar{\sigma}_1 \\ \bar{\sigma}_2 \end{Bmatrix}, \quad \bar{\boldsymbol{\varepsilon}} := \begin{Bmatrix} \bar{\varepsilon}_1 \\ \bar{\varepsilon}_2 \end{Bmatrix}, \quad \nabla := \begin{Bmatrix} \frac{\partial}{\partial x_1} \\ \frac{\partial}{\partial x_2} \end{Bmatrix} \quad (9)$$

and

$$\tilde{\Lambda} = \mathbf{Q} \tilde{\Lambda}' \mathbf{Q}^T, \quad \Lambda = \mathbf{Q} \Lambda' \mathbf{Q}^T \quad (10)$$

with

$$\tilde{\Lambda}' := \begin{bmatrix} \lambda_2(x'_2) & \cdot \\ \cdot & \lambda_1(x'_1) \end{bmatrix}, \quad \Lambda' := \begin{bmatrix} 1/\lambda_1(x'_1) & \cdot \\ \cdot & 1/\lambda_2(x'_2) \end{bmatrix} \quad (11)$$

Equation (8) explicitly incorporates Voigt material damping through the correspondence principle in terms of a damping ratio ζ and a non-dimensional frequency $a_0 = k_s b$, where b is a characteristic length of the physical problem. This damping model is chosen over the traditional hysteretic damping model because the latter is non-causal [32]; implementation of a causal hysteretic model in a PML formulation is beyond the scope of this paper.

Because multiplication or division by the factor $i\omega$ in the frequency domain corresponds to a derivative or an integral, respectively, in the time domain, time-harmonic equations are easily transformed into corresponding equations for transient motion if the frequency-dependence of the former is only a simple dependence on this factor. Therefore, the stretching functions are chosen to be of the form

$$\lambda_i(x'_i) := [1 + f_i^e(x'_i)] - i \frac{f_i^p(x'_i)}{k_s} \quad (12)$$

where, the functions f_i^e serve to attenuate evanescent waves whereas the functions f_i^p serve to attenuate propagating waves. For λ_i as in Eq. (12), the stretch tensors $\tilde{\Lambda}$ and Λ can be written as

$$\tilde{\Lambda} = \tilde{\mathbf{F}}^e + \frac{1}{i\omega} \tilde{\mathbf{F}}^p, \quad \Lambda = \left[\mathbf{F}^e + \frac{1}{i\omega} \mathbf{F}^p \right]^{-1} \quad (13)$$

where

$$\tilde{\mathbf{F}}^e = \mathbf{Q} \tilde{\mathbf{F}}^{e'} \mathbf{Q}^T, \quad \tilde{\mathbf{F}}^p = \mathbf{Q} \tilde{\mathbf{F}}^{p'} \mathbf{Q}^T, \quad \mathbf{F}^e = \mathbf{Q} \mathbf{F}^{e'} \mathbf{Q}^T, \quad \mathbf{F}^p = \mathbf{Q} \mathbf{F}^{p'} \mathbf{Q}^T \quad (14)$$

with

$$\tilde{\mathbf{F}}^{e'} := \begin{bmatrix} 1 + f_2^e(x'_2) & \cdot \\ \cdot & 1 + f_1^e(x'_1) \end{bmatrix}, \quad \tilde{\mathbf{F}}^{p'} := \begin{bmatrix} c_s f_2^p(x'_2) & \cdot \\ \cdot & c_s f_1^p(x'_1) \end{bmatrix} \quad (15a)$$

and

$$\mathbf{F}^{e'} := \begin{bmatrix} 1 + f_1^e(x'_1) & \cdot \\ \cdot & 1 + f_2^e(x'_2) \end{bmatrix}, \quad \mathbf{F}^{p'} := \begin{bmatrix} c_s f_1^p(x'_1) & \cdot \\ \cdot & c_s f_2^p(x'_2) \end{bmatrix} \quad (15b)$$

Equation (8c) is premultiplied by $i\omega \Lambda^{-1}$, Eqs. (12) and (13) are substituted into Eq. (8), and the inverse Fourier transform is applied to the resultant to obtain the time domain equations for the PML:

$$\nabla \cdot \tilde{\boldsymbol{\sigma}} = \rho f_m \ddot{u} + \rho c_s f_c \dot{u} + \mu f_k u \quad (16a)$$

$$\boldsymbol{\sigma} = \mu \left(\boldsymbol{\varepsilon} + \frac{2\zeta b}{c_s} \dot{\boldsymbol{\varepsilon}} \right) \quad (16b)$$

$$\mathbf{F}^e \dot{\boldsymbol{\varepsilon}} + \mathbf{F}^p \boldsymbol{\varepsilon} = \nabla \dot{u} \quad (16c)$$

where

$$\tilde{\boldsymbol{\sigma}} := \tilde{\mathbf{F}}^e \boldsymbol{\sigma} + \tilde{\mathbf{F}}^p \boldsymbol{\Sigma}, \quad \text{with} \quad \boldsymbol{\Sigma} := \int_0^t \boldsymbol{\sigma} \, d\tau \quad (17)$$

and

$$\begin{aligned} f_m &:= [1 + f_1^e(x'_1)][1 + f_2^e(x'_2)], \\ f_c &:= [1 + f_1^e(x'_1)]f_2^p(x'_2) + [1 + f_2^e(x'_2)]f_1^p(x'_1), \\ f_k &:= f_1^p(x'_1)f_2^p(x'_2) \end{aligned} \quad (18)$$

The application of the inverse Fourier transform to obtain Σ assumes that $\tilde{\sigma}(\omega = 0) = 0$. The presence of the time-integral of σ in the governing equations, although unconventional from the point-of-view of continuum mechanics, is not unnatural in a time-domain implementation of a PML obtained without field-splitting [33].

2.4. Finite element implementation

Equation (16) is implemented using a standard displacement-based finite element approach [34]. The weak form of Eq. (16a) is derived by multiplying it with an arbitrary weighting function w residing in an appropriate admissible space, and then integrating over the entire computational domain Ω using integration-by-parts and the divergence theorem to obtain

$$\int_{\Omega} \rho f_m w \ddot{u} \, d\Omega + \int_{\Omega} \rho c_s f_c w \dot{u} \, d\Omega + \int_{\Omega} \mu f_k w u \, d\Omega + \int_{\Omega} \nabla w \cdot \tilde{\sigma} \, d\Omega = \int_{\Gamma} w \tilde{\sigma} \cdot \mathbf{n} \, d\Gamma \quad (19)$$

where $\Gamma := \partial\Omega$ is the boundary of Ω and \mathbf{n} is the unit normal to Γ . The weak form is first spatially discretised by interpolating u and w element-wise in terms of nodal quantities using appropriate nodal shape functions. This leads to the system of equations

$$\mathbf{m}\ddot{\mathbf{d}} + \mathbf{c}\dot{\mathbf{d}} + \mathbf{k}\mathbf{d} + \mathbf{p}_{\text{int}} = \mathbf{p}_{\text{ext}} \quad (20)$$

where \mathbf{m} , \mathbf{c} and \mathbf{k} are the mass, damping and stiffness matrices, respectively, \mathbf{d} is a vector of nodal displacements, \mathbf{p}_{int} is a vector of internal force terms, and \mathbf{p}_{ext} is a vector of external forces. These matrices and vectors are assembled from corresponding element-level matrices and vectors. In particular, the element-level constituent matrices of \mathbf{m} , \mathbf{c} and \mathbf{k} are, respectively,

$$\mathbf{m}^e = \int_{\Omega^e} \rho f_m \mathbf{N}^T \mathbf{N} \, d\Omega, \quad \mathbf{c}^e = \int_{\Omega^e} \rho c_s f_c \mathbf{N}^T \mathbf{N} \, d\Omega, \quad \mathbf{k}^e = \int_{\Omega^e} \mu f_k \mathbf{N}^T \mathbf{N} \, d\Omega \quad (21a)$$

and the element-level internal force term is

$$\mathbf{p}^e = \int_{\Omega^e} \mathbf{B}^T \tilde{\sigma} \, d\Omega \quad (21b)$$

where \mathbf{N} is a row vector of element-level nodal shape functions, and

$$\mathbf{B} = \begin{bmatrix} \mathbf{N}_{,1} \\ \mathbf{N}_{,2} \end{bmatrix} \quad (22)$$

The functions f_i^e and f_i^p are defined globally on the computational domain, not element-wise. It is conveniently assumed that $\tilde{\boldsymbol{\sigma}} \cdot \mathbf{n} = 0$ on a free boundary of the PML.

Equation (20) can be solved using a time-stepping algorithm such as the Newmark method [35, 36], alongwith Newton-Raphson iteration at each time step to enforce equilibrium. If Eq. (20) is solved, say, at time station t_{n+1} , given the solution at t_n , the Newton-Raphson iteration at this time step will require a) calculation of $\tilde{\boldsymbol{\sigma}}_{n+1}$, for calculating \mathbf{p}_{n+1}^e [$\approx \mathbf{p}^e(t_{n+1})$], and b) a consistent linearisation [34, vol. 2] of \mathbf{p}_{n+1}^e at \mathbf{d}_{n+1} [$\approx \mathbf{d}^e(t_{n+1})$], where \mathbf{d}^e is a vector of element-level nodal displacements. Therefore, Eq. (16c) is discretised using a backward Euler scheme on $\boldsymbol{\varepsilon}$ to obtain

$$\boldsymbol{\varepsilon}_{n+1} = \left[\frac{\mathbf{F}^e}{\Delta t} + \mathbf{F}^p \right]^{-1} \left[\mathbf{B}\mathbf{v}_{n+1} + \frac{\mathbf{F}^e}{\Delta t} \boldsymbol{\varepsilon}_n \right] \quad (23)$$

where $\mathbf{v}_{n+1} \approx \dot{\mathbf{d}}^e(t_{n+1})$, and Δt is the time-step size. A similar time-discretisation of Eq. (16b) gives

$$\boldsymbol{\sigma}_{n+1} = \mu \left(1 + \frac{2\zeta b}{c_s \Delta t} \right) \boldsymbol{\varepsilon}_{n+1} - \mu \frac{2\zeta b}{c_s \Delta t} \boldsymbol{\varepsilon}_n \quad (24)$$

Furthermore, Eq. (17b) is used to approximate $\boldsymbol{\Sigma}_{n+1}$ as

$$\boldsymbol{\Sigma}_{n+1} = \boldsymbol{\Sigma}_n + \boldsymbol{\sigma}_{n+1} \Delta t \quad (25)$$

Equation (25) is substituted in Eq. (17a) to obtain

$$\tilde{\boldsymbol{\sigma}}_{n+1} = \Delta t \left[\frac{\tilde{\mathbf{F}}^e}{\Delta t} + \tilde{\mathbf{F}}^p \right] \boldsymbol{\sigma}_{n+1} + \tilde{\mathbf{F}}^p \boldsymbol{\Sigma}_n \quad (26)$$

This gives the internal force term

$$\mathbf{p}_{n+1}^e = \int_{\Omega^e} \mathbf{B}^T \tilde{\boldsymbol{\sigma}}_{n+1} d\Omega \quad (27)$$

Linearisation of Eq. (27) gives

$$\Delta \mathbf{p}_{n+1}^e = \left[\int_{\Omega^e} \mathbf{B}^T \mathbf{D} \mathbf{B} d\Omega \right] \Delta \mathbf{v}_{n+1} \quad (28)$$

where Δ is the differential operator, and

$$\mathbf{D} = \mu \Delta t \left(1 + \frac{2\zeta b}{c_s \Delta t} \right) \left[\frac{\tilde{\mathbf{F}}^e}{\Delta t} + \tilde{\mathbf{F}}^p \right] \left[\frac{\mathbf{F}^e}{\Delta t} + \mathbf{F}^p \right]^{-1} \quad (29)$$

i.e., this linearisation gives a tangent matrix

$$\check{\mathbf{c}}^e := \int_{\Omega^e} \mathbf{B}^T \mathbf{D} \mathbf{B} d\Omega \quad (30)$$

which may be incorporated into the effective tangent stiffness used in the time-stepping algorithm.

A skeleton of the algorithm for computing the element-level effective internal force and tangent stiffness is given in Box I. The matrix $\check{\mathbf{c}}^e$ is symmetric because \mathbf{D} is symmetric by the virtue of the coaxiality of the constituent matrices. The other system matrices, \mathbf{m} , \mathbf{c} and \mathbf{k} are clearly symmetric by Eq. (21a). Moreover, because all these matrices are of the same form as the system matrices for an elastic medium, the effective tangent stiffness (say, as found in the Newmark scheme) of the entire computational domain will be positive definite if f_i^e and f_i^p are positive and if the boundary restraints are adequate. Furthermore, since all the system matrices, \mathbf{m} , \mathbf{c} , $\check{\mathbf{c}}$ and \mathbf{k} that constitute the tangent stiffness are independent of \mathbf{d} , this is effectively a linear model.

Box I. Computing effective force and stiffness for anti-plane PML element.

1. Compute system matrices \mathbf{m}^e , \mathbf{c}^e and \mathbf{k}^e [Eq. (21a)].
2. Compute internal force \mathbf{p}_{n+1}^e [Eq. (27)].
Use $\boldsymbol{\varepsilon}_{n+1}$ [Eq. (23)], $\boldsymbol{\sigma}_{n+1}$ [Eq. (24)] and $\tilde{\boldsymbol{\sigma}}_{n+1}$ [Eq. (26)].
3. Compute tangent matrix $\check{\mathbf{c}}^e$ [Eq. (30)] using \mathbf{D} [Eq. (29)].
4. Compute effective internal force $\tilde{\mathbf{p}}_{n+1}^e$ and tangent stiffness $\tilde{\mathbf{k}}^e$:

$$\begin{aligned}\tilde{\mathbf{p}}_{n+1}^e &= \mathbf{m}^e \mathbf{a}_{n+1} + \mathbf{c}^e \mathbf{v}_{n+1} + \mathbf{k}^e \mathbf{d}_{n+1} + \mathbf{p}_{n+1}^e \\ \tilde{\mathbf{k}}^e &= \alpha_k \mathbf{k}^e + \alpha_c (\mathbf{c}^e + \check{\mathbf{c}}^e) + \alpha_m \mathbf{m}^e\end{aligned}$$

where $\mathbf{a}_{n+1} \approx \ddot{\mathbf{d}}^e(t_{n+1})$, and, for example,

$$\alpha_k = 1, \quad \alpha_c = \frac{\gamma}{\beta \Delta t}, \quad \alpha_m = \frac{1}{\beta \Delta t^2}$$

for the Newmark method.

Note: The tangent stiffness $\tilde{\mathbf{k}}^e$ is independent of the solution, and thus has to be computed only once. However, the internal force \mathbf{p}_{n+1}^e has to be re-computed at each time-step because it is dependent on the solution at past times.

2.5. Numerical results

Consider a homogeneous isotropic semi-infinite layer of depth d on a rigid base, as shown in Fig. 2(a), whose anti-plane motion is governed by Eq. (1) with the following boundary conditions:

$$\begin{aligned} u(\mathbf{x}, t) &= 0 && \text{at } x_2 = 0, \forall x_1 > 0, \forall t \\ \sigma_2 &= 0 && \text{at } x_2 = d, \forall x_1 > 0, \forall t \\ u(\mathbf{x}, t) &= u_1(t)N_1(x_2/d) + u_2(t)N_2(x_2/d) && \text{at } x_1 = 0, \forall x_2 \in [0, d] \end{aligned} \quad (31)$$

and a radiation condition for $x_1 \rightarrow \infty$, where u_1 and u_2 are the displacements at nodes 1 and 2, and N_1 and N_2 are shape functions defined as

$$N_1(\xi) = 4\xi(1 - \xi), \quad N_2(\xi) = \xi(2\xi - 1), \quad \xi \in [0, 1]. \quad (32)$$

The wave motion in this system is similar to Love wave motion: it is dispersive, and consists of not only propagating modes but also an infinite number of evanescent modes, with the propagation (and decay) in the x_1 -direction [37, App. A.3].

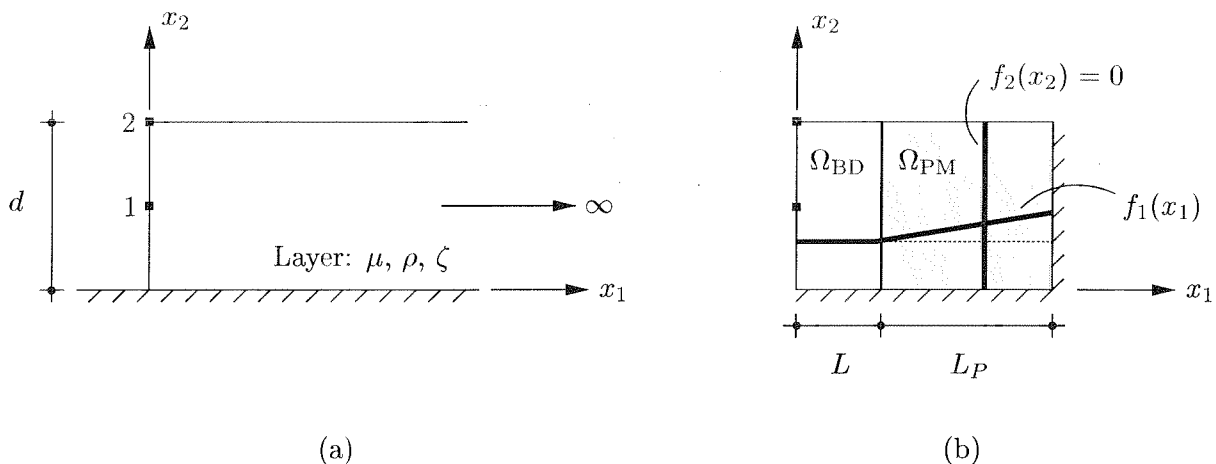


Figure 2. (a) Homogeneous isotropic (visco-)elastic semi-infinite layer of depth d on a fixed base; (b) a PML model.

The time-domain response of this system may be studied through the reactions at nodes 1 and 2 due to any combination of nodal displacements $u_1(t)$ and $u_2(t)$. Here, an inverted cosine pulse, given by

$$\begin{aligned} u_0(t) &= \frac{1}{2} \left[1 - \cos \left(2\pi \frac{t}{t_d} \right) \right] && t \in [0, t_d] \\ &= 0 && t \in (t_d, \infty) \end{aligned} \quad (33)$$

and shown in Fig. 3(a), is applied to the two nodes individually, i.e., two cases are considered: 1) $u_1(t) = u_0(t)$, $u_2(t) \equiv 0$, and 2) $u_1(t) \equiv 0$, $u_2(t) = u_0(t)$, and the two nodal reactions are computed for each of the two excitations. The exact solution for these reactions can be computed through convolution with the unit-impulse response [37].

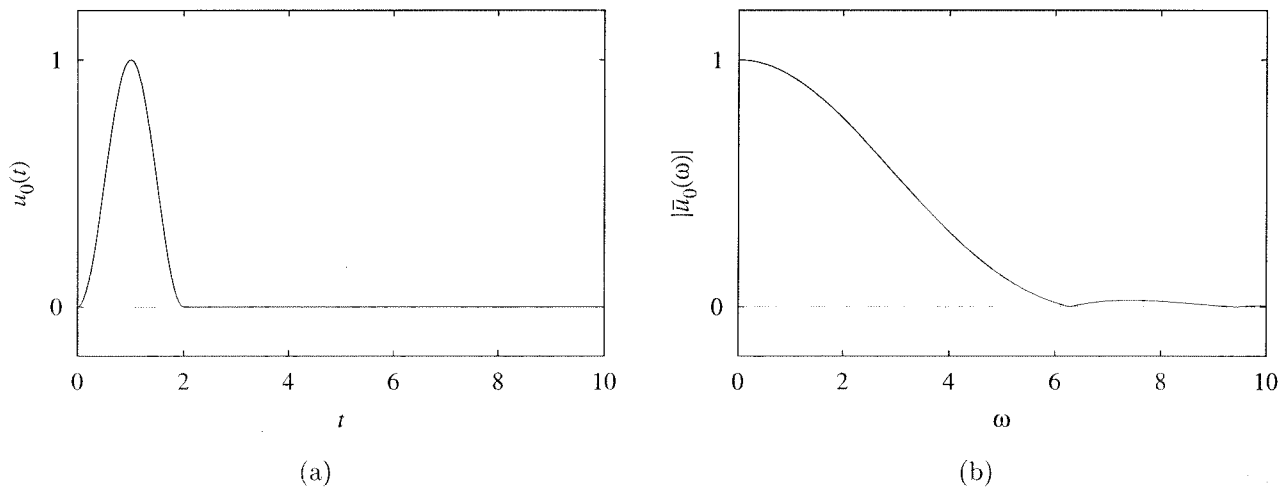


Figure 3. Plot of (a) input displacement: Eq. (33) for $t_d = 2$; (b) amplitude of its Fourier transform.

This semi-infinite layer is modelled using the bounded-domain-PML model shown in Fig. 2(b), composed of a bounded domain Ω_{BD} and a PML Ω_{PM} , with the attenuation functions in Eq. (12) chosen as $f_1^e = f_1^p = f$, where f is linear in the PML, and $f_2^e = f_2^p = 0$. A uniform finite element mesh of four-node bilinear isoparametric elements is used to discretise the entire bounded domain. The mesh is chosen to have n_d elements per unit d , n_b elements per unit L/d across the width of Ω_{BD} , and n_p elements per unit L_P/d across Ω_{PM} , with choices for n_d , n_b and n_p indicated along with the numerical results. For comparison, the layer is also modelled using viscous dashpots [4], with consistent dashpots placed at the edge $x_1 = L + L_P$, and the entire domain $\Omega_{\text{BD}} \cup \Omega_{\text{PM}}$ taken to be elastic. Thus, the domain size and mesh size are comparable to those in the PML model.

Figure 4(a) presents the nodal reactions computed for an elastic medium using the PML model and the dashpot model against the exact reactions computed using convolution of the excitation and the exact impulse response function in Ref. 37, where P_{ij} denotes the reaction at node i due to a nonzero displacement at node j . The results obtained from the PML model are virtually indistinguishable from the exact results, even though the domain is small enough that the viscous-dashpot boundary reflects waves back to $x_1 = 0$ within the time-interval considered. Moreover, these accurate results from the PML model are obtained at a low computational cost: the cost of the PML model is only slightly larger than that of

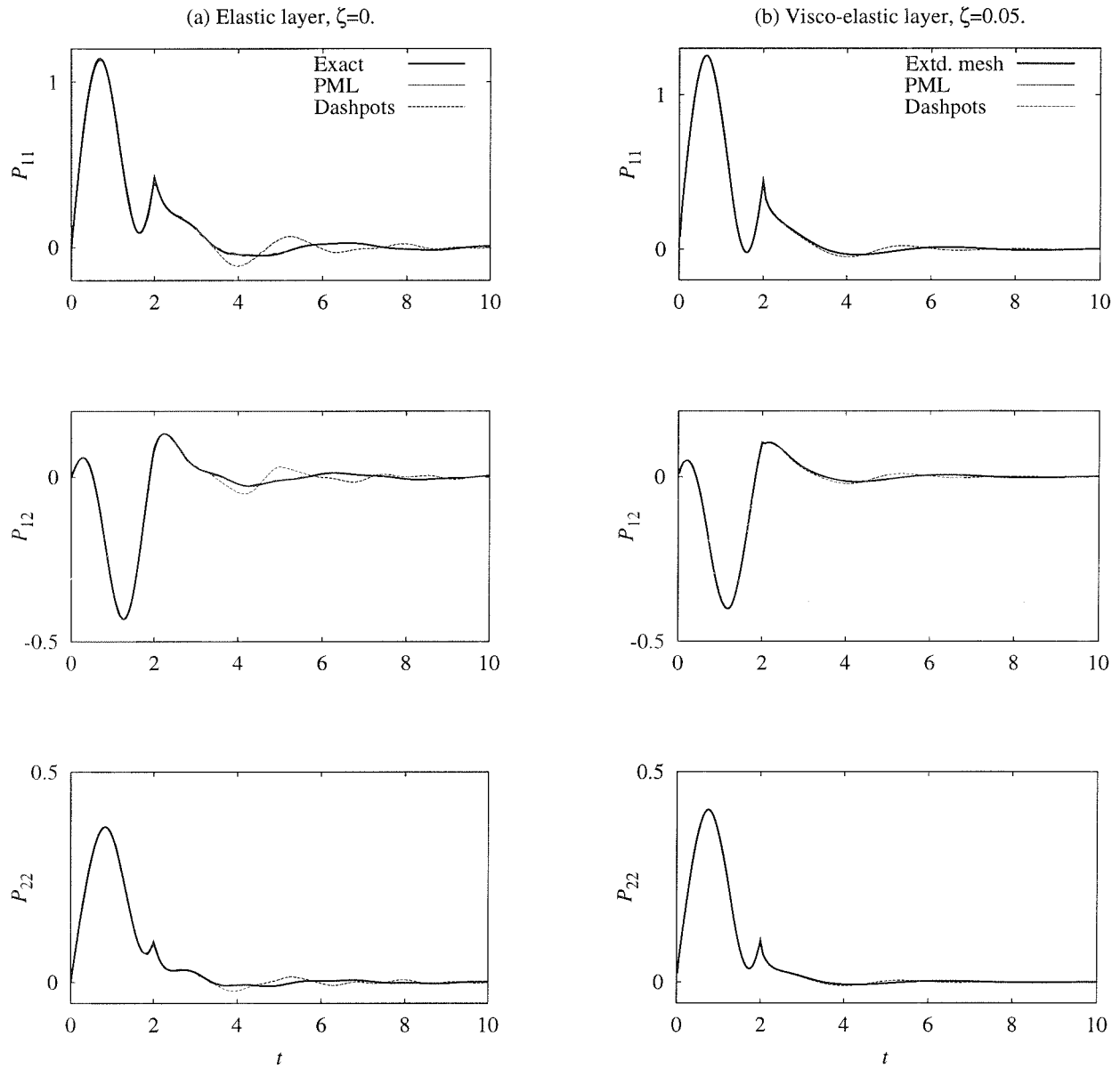


Figure 4. Nodal reactions of (visco-)elastic semi-infinite layer on fixed base, due to imposed nodal displacements; $L = d/2$, $L_P = d$, $n_b = n_p = 15$, $n_d = 15$, $f_1(x_1) = 10\langle x_1 - L \rangle / L_P$; $t_d = 2$, $\Delta t = 0.02$.

the dashpot model. Figure 4(b) presents similar results for a visco-elastic layer, with results from an extended-mesh model used as a benchmark in the absence of analytical solutions; this extended-mesh model is a viscous-dashpot model of depth d and length $10d$ from the edge $x_1 = 0$, with consistent dashpots at $x_1 = 10d$ and visco-elastic material within the domain. The results from the PML model are highly accurate, even though the computational domain is small: the dashpot model generates spurious reflections even for a visco-elastic medium.

2.6. *Caveat emptor*

The time-domain equations for the PML were obtained by a special choice of the stretching functions — Eq. (12) — that enabled transformation of the frequency domain PML equations into the time domain. However, these stretching functions differ from those used for frequency-domain analysis in Ref. 30, where they were chosen as

$$\lambda_i(x'_i) := \left[1 + \frac{f_i^e(x'_i)}{k_s^*} \right] - i \frac{f_i^p(x'_i)}{k_s^*} \quad (34)$$

where, e.g., $k_s^* = k_s / \sqrt{1 + 2ia_0\zeta}$ for the Voigt damping model; these stretching functions produced accurate results in the frequency domain, even for problems with significant evanescent modes in their wave motion.

Because the real part of the complex-valued stretching function serves to attenuate evanescent waves, and because, for an elastic medium the difference between the time-domain and the frequency-domain stretching functions is only in the real part, it is valid to ask whether the time-domain stretching functions are adequate for evanescent waves. Note that it is difficult to employ the frequency-domain stretching function [Eq. (34)] towards a time-domain model, even for an elastic medium, because the frequency-dependence of the real part of the stretching function is not through the factor $i\omega$. Because the PML approach is fundamentally a frequency-domain approach, it is valid to test the adequacy of the time-domain stretching function [Eq. (12)] by using it to obtain frequency-domain results.

The frequency-domain response of this layer on a half-plane can be characterised by the amplitude of nodal forces due to unit-amplitude harmonic motion at either node. The force amplitude at node i due to a unit-amplitude displacement at node j with frequency $a_0 = k_s d$ is denoted by $S_{ij}(a_0)$ and is decomposed into stiffness and damping coefficients k_{ij} and c_{ij} as

$$S_{ij}(a_0) = S_{ij}(0) [k_{ij}(a_0) + ia_0 c_{ij}(a_0)] \quad (\text{no summation}) \quad (35)$$

Analytical, closed-form expressions for $S_{ij}(a_0)$ is available in Appendix A.3 of Ref. 37.

Figure 5 compares results for an elastic layer obtained from PML models using the two stretching functions against analytical results [37]. The mesh used for the PML models is the same as those used for time-domain analysis; the results are obtained using the frequency-domain FE formulation presented in Ref. 30. It is seen that the frequency-domain-only stretching function [Eq. (34)] produces highly accurate results, denoted by “FD PML”,

whereas the time-domain stretching function [Eq. (12)] produces results, denoted by “PML” that are inaccurate for $a_0 > 6$. This suggests that the time-domain stretching function cannot adequately attenuate evanescent waves, which is supported by Fig. 6, showing results for a visco-elastic layer obtained using a PML model with the time-domain stretching function: the material damping attenuates the evanescent modes, and the results are now highly accurate. The exact results in Fig. 6 are obtained by applying the correspondence principle to the corresponding closed-form expressions for an elastic layer [37].

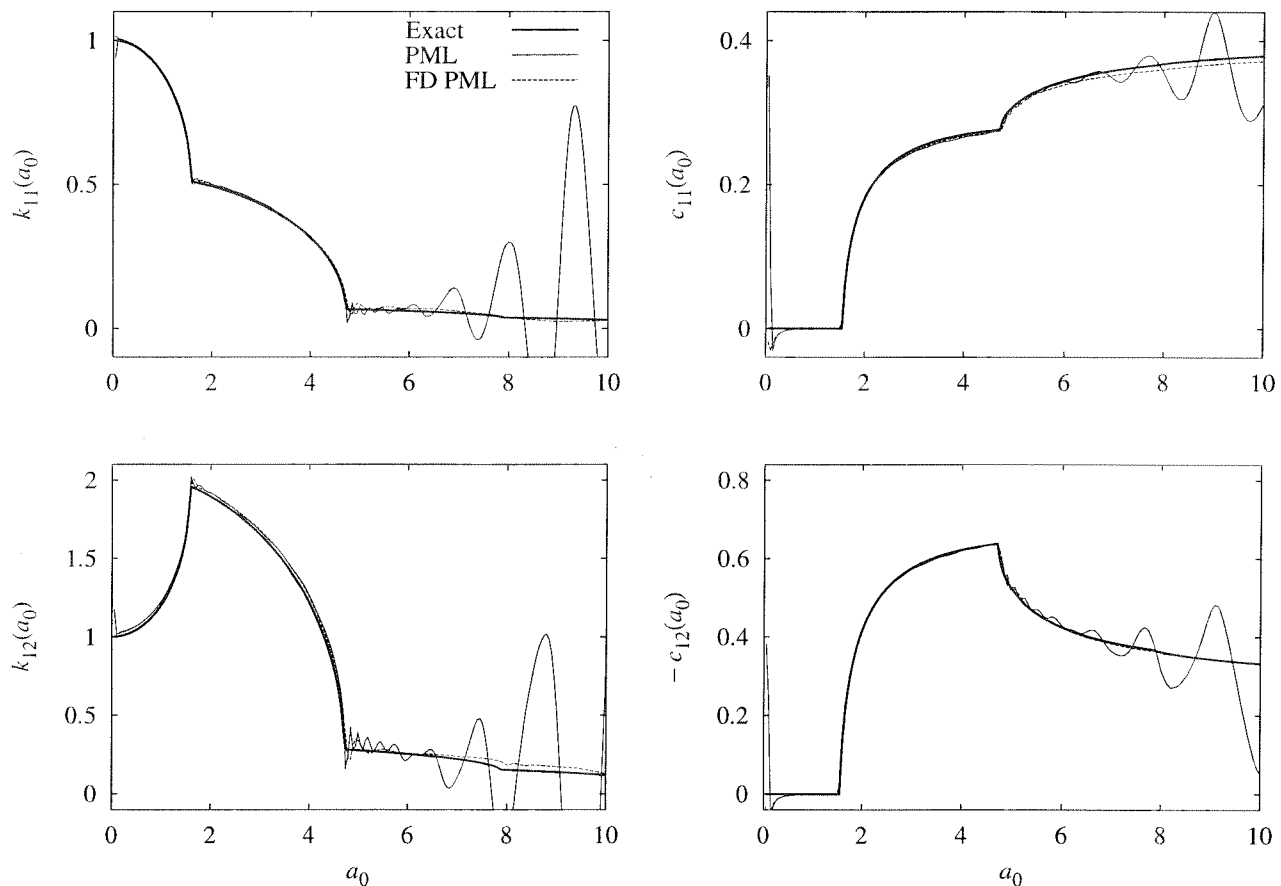


Figure 5. Dynamic stiffness coefficients of elastic semi-infinite layer on fixed base computed using PML models with two different forms of the stretching function: “PML” from a stretching function that can be implemented in the time domain, and “FD PML” from a stretching function that is more accurate but is only suitable for the frequency domain; $L = d/2$, $L_P = d$, $n_b = n_p = 15$, $n_d = 15$, $f_1(x_1) = 10(x_1 - L)/L_P$; “Exact” results from Ref. 37.

Thus, for undamped systems with severely-constricted geometries — typically, waveguides such as the layer on a rigid base — the time domain results from a PML model may not be accurate if the excitation is primarily in a frequency band where evanescent modes

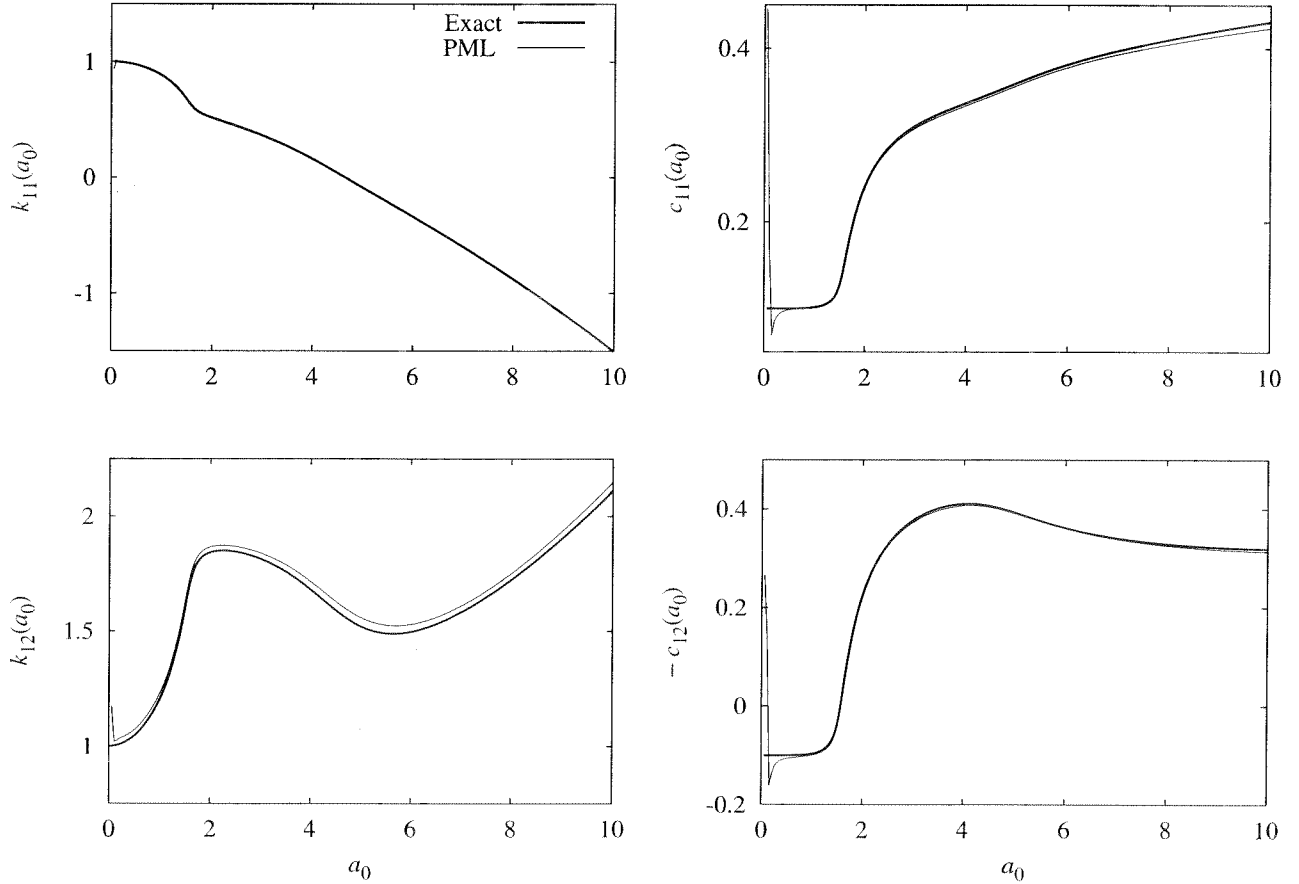


Figure 6. Dynamic stiffness coefficients of visco-elastic semi-infinite layer on fixed base computed using a PML model with a stretching function that can be implemented in the time domain; $L = d/2$, $L_P = d$, $n_b = n_p = 15$, $n_d = 15$, $f_1(x_1) = 10\langle x_1 - L \rangle / L_P$; $\zeta = 0.05$; “Exact” results through the correspondence principle.

are dominant. Such a conclusion is echoed in electromagnetics literature [38, 39], where alternative choices of the stretching function have been considered for attenuating evanescent waves. The transient PML response shown in Fig. 4(a) is accurate because the dominant frequencies in the applied displacement [Eq. (33)] are below $a_0 = 6$ for $t_d = 2$; see Fig. 3(b).

3. PLANE-STRAIN MOTION

3.1. Elastic medium

Consider a homogeneous isotropic elastic medium undergoing plane-strain motion in the absence of body forces. The displacements $\mathbf{u}(\mathbf{x}, t)$ of such a medium are governed by the following equations ($i, j, k, l \in \{1, 2\}$):

$$\sum_j \frac{\partial \sigma_{ij}}{\partial x_j} = \rho \ddot{u}_i, \quad (36a)$$

$$\sigma_{ij} = \sum_{k,l} C_{ijkl} \varepsilon_{kl}, \quad (36b)$$

$$\varepsilon_{ij} = \frac{1}{2} \left[\frac{\partial u_i}{\partial x_j} + \frac{\partial u_j}{\partial x_i} \right] \quad (36c)$$

where C_{ijkl} written in terms of the Kronecker delta δ_{ij} is

$$C_{ijkl} = \left(\kappa - \frac{2}{3}\mu \right) \delta_{ij}\delta_{kl} + \mu (\delta_{ik}\delta_{jl} + \delta_{il}\delta_{jk}) \quad (37)$$

σ_{ij} and ε_{ij} are the components of $\boldsymbol{\sigma}$ and $\boldsymbol{\varepsilon}$, the stress and infinitesimal strain tensors, C_{ijkl} are the components of \mathbf{C} , the material stiffness tensor; κ is the bulk modulus, μ the shear modulus, and ρ the mass density of the medium. Equation (36) also describes plane-stress motion if κ is re-defined appropriately.

On an unbounded domain, Eq. (36) admits body-wave solutions [31] in the form of 1) P waves:

$$\mathbf{u}(\mathbf{x}, t) = \mathbf{q} \exp[-ik_p \mathbf{x} \cdot \mathbf{p}] \exp(i\omega t) \quad (38a)$$

where $k_p = \omega/c_p$, with $c_p = \sqrt{(\kappa + 4\mu/3)/\rho}$ the P-wave speed, \mathbf{p} is a unit vector denoting the propagation direction, and $\mathbf{q} = \pm \mathbf{p}$ the direction of particle motion, and 2) S waves:

$$\mathbf{u}(\mathbf{x}, t) = \mathbf{q} \exp[-ik_s \mathbf{x} \cdot \mathbf{p}] \exp(i\omega t) \quad (38b)$$

where $k_s = \omega/c_s$, with $c_s = \sqrt{\mu/\rho}$ the S-wave speed, and $\mathbf{q} \cdot \mathbf{p} = 0$.

3.2. Perfectly matched layer

The discussion presented here is a synopsis of the corresponding development in Ref. 30. The summation convention is abandoned in this section.

A PML for plane-strain motion is defined naturally in the frequency domain as

$$\sum_j \frac{1}{\lambda_j(x_j)} \frac{\partial \bar{\sigma}_{ij}}{\partial x_j} = -\omega^2 \rho \bar{u}_i, \quad (39a)$$

$$\bar{\sigma}_{ij} = \sum_{k,l} C_{ijkl} \bar{\varepsilon}_{kl}, \quad (39b)$$

$$\bar{\varepsilon}_{ij} = \frac{1}{2} \left[\frac{1}{\lambda_j(x_j)} \frac{\partial \bar{u}_i}{\partial x_j} + \frac{1}{\lambda_i(x_i)} \frac{\partial \bar{u}_j}{\partial x_i} \right] \quad (39c)$$

where λ_i are nowhere-zero, continuous, complex-valued coordinate stretching functions. Because the constitutive relation Eq. (39b) is the same as for the elastic medium, Eq. (39) also describes a PMM for plane-stress motion if κ is re-defined appropriately. Equation (39) assumes harmonic time-dependence of the displacement, stress and strain, e.g., $\mathbf{u}(\mathbf{x}, t) = \bar{\mathbf{u}}(\mathbf{x}) \exp(i\omega t)$, where ω is the frequency of excitation.

If the stretching functions are chosen as in Eq. (4), then Eq. (39) admits solutions of the form

$$\bar{\mathbf{u}}(\mathbf{x}) = \exp \left[-\frac{c_s}{c_p} \sum_i F_i(x_i) p_i \right] \mathbf{q} \exp[-ik_p \mathbf{x} \cdot \mathbf{p}] \quad (40a)$$

with $\mathbf{q} = \pm \mathbf{p}$, and

$$\bar{\mathbf{u}}(\mathbf{x}) = \exp \left[-\sum_i F_i(x_i) p_i \right] \mathbf{q} \exp[-ik_s \mathbf{x} \cdot \mathbf{p}] \quad (40b)$$

with $\mathbf{q} \cdot \mathbf{p} = 0$, and F_i defined as in Eq. (6). Thus, if $F_i(x_i) > 0$ and $p_i > 0$, then the wave solutions admitted in the PML medium are P-type and S-type waves, but with a spatial attenuation imposed upon them.

As in the case of anti-plane motion, an appropriately defined PML may be placed adjacent to a bounded domain (Fig. 1) in order to simulate an unbounded domain. A wave travelling outwards from the bounded domain is absorbed into the PML without any reflection from the bounded-domain-PML interface. This wave is then attenuated in the layer and reflected back from the fixed end towards the bounded domain. For example, an incident P wave of unit amplitude will be reflected back from the fixed end as a P wave and an S wave, and their amplitudes, as they exit the PML, will be [30],

$$\begin{aligned} |R_{pp}| &= \frac{\cos(\theta + \theta_s)}{\cos(\theta - \theta_s)} \exp \left[-2 \frac{c_s}{c_p} F_1(L_P) \cos \theta \right], \\ |R_{sp}| &= \frac{\sin 2\theta}{\cos(\theta - \theta_s)} \exp \left[-F_1(L_P) \left(\frac{c_s}{c_p} \cos \theta + \cos \theta_s \right) \right] \end{aligned} \quad (41)$$

with θ_s given by

$$\sin \theta_s = \frac{c_s}{c_p} \sin \theta$$

These reflected-wave amplitudes are controlled by the choice of the attenuation function and the depth of the layer, and can be made arbitrarily small for non-tangentially incident waves. Because outgoing waves in such a system will be only minimally reflected back towards the interface, such a bounded-domain-PML system is an appropriate model for the corresponding unbounded-domain system.

3.3. Time-domain equations for the PML

Equation (39) represents a PML wherein waves are attenuated in the x_1 and x_2 directions. As in the case of anti-plane motion, the equations for the plane-strain PML can be rewritten to represent a medium wherein the attenuation is in two arbitrary (orthogonal) directions [30]:

$$\operatorname{div} \left(\bar{\boldsymbol{\sigma}} \tilde{\boldsymbol{\Lambda}} \right) = -\omega^2 \rho [\lambda_1(x'_1) \lambda_2(x'_2)] \bar{\mathbf{u}}, \quad (42a)$$

$$\bar{\boldsymbol{\sigma}} = (1 + 2ia_0\zeta) \mathbf{C} \bar{\boldsymbol{\varepsilon}}, \quad (42b)$$

$$\bar{\boldsymbol{\varepsilon}} = \frac{1}{2} \left[(\operatorname{grad} \bar{\mathbf{u}}) \boldsymbol{\Lambda} + \boldsymbol{\Lambda}^T (\operatorname{grad} \bar{\mathbf{u}})^T \right] \quad (42c)$$

where $\tilde{\boldsymbol{\Lambda}}$ and $\boldsymbol{\Lambda}$ are as in Eqs. (10)–(11). Equation (42) explicitly incorporates Voigt material damping through the correspondence principle in terms of a damping ratio ζ and a non-dimensional frequency $a_0 = k_s b$, where b is a characteristic length of the physical problem.

Choosing the stretching functions to be of the form in Eq. (12) allows transformation of Eq. (42) into the time domain. Equation (42c) is premultiplied by $i\omega \boldsymbol{\Lambda}^{-T}$ and postmultiplied by $\boldsymbol{\Lambda}^{-1}$, Eqs. (12) and (13) are substituted into Eq. (42), and the inverse Fourier transform is applied to the resultant to obtain the time domain equations for the PML:

$$\operatorname{div} \left(\boldsymbol{\sigma} \tilde{\mathbf{F}}^e + \boldsymbol{\Sigma} \tilde{\mathbf{F}}^p \right) = \rho f_m \ddot{\mathbf{u}} + \rho c_s f_c \dot{\mathbf{u}} + \mu f_k \mathbf{u}, \quad (43a)$$

$$\boldsymbol{\sigma} = \mathbf{C} \left(\boldsymbol{\varepsilon} + \frac{2\zeta b}{c_s} \dot{\boldsymbol{\varepsilon}} \right), \quad (43b)$$

$$\begin{aligned} \mathbf{F}^{eT} \dot{\boldsymbol{\varepsilon}} \mathbf{F}^e + (\mathbf{F}^{pT} \boldsymbol{\varepsilon} \mathbf{F}^e + \mathbf{F}^{eT} \boldsymbol{\varepsilon} \mathbf{F}^p) + \mathbf{F}^{pT} \mathbf{E} \mathbf{F}^p = \\ \frac{1}{2} \left[\mathbf{F}^{eT} (\operatorname{grad} \dot{\mathbf{u}}) + (\operatorname{grad} \dot{\mathbf{u}})^T \mathbf{F}^e \right] + \frac{1}{2} \left[\mathbf{F}^{pT} (\operatorname{grad} \mathbf{u}) + (\operatorname{grad} \mathbf{u})^T \mathbf{F}^p \right] \end{aligned} \quad (43c)$$

where $\tilde{\mathbf{F}}^e$, $\tilde{\mathbf{F}}^p$, \mathbf{F}^e and \mathbf{F}^p are as in Eqs. (14)–(15), f_m , f_c and f_k are as in Eq. (18), and

$$\boldsymbol{\Sigma} := \int_0^t \boldsymbol{\sigma} \, d\tau, \quad \mathbf{E} := \int_0^t \boldsymbol{\varepsilon} \, d\tau \quad (44)$$

Application of the inverse Fourier transform to obtain $\boldsymbol{\Sigma}$ and \mathbf{E} assumes that $\bar{\boldsymbol{\sigma}}(\omega = 0) = 0$ and $\bar{\boldsymbol{\varepsilon}}(\omega = 0) = 0$.

3.4. Finite element implementation

Equation (43) is implemented using a standard displacement-based finite element approach [34]. The weak form of Eq. (43a) is derived by taking its inner product with an arbitrary weighting function \mathbf{w} residing in an appropriate admissible space, and then integrating over the entire computational domain Ω using integration-by-parts and the divergence theorem to obtain

$$\int_{\Omega} \rho f_m \mathbf{w} \cdot \ddot{\mathbf{u}} \, d\Omega + \int_{\Omega} \rho c_s f_c \mathbf{w} \cdot \dot{\mathbf{u}} \, d\Omega + \int_{\Omega} \mu f_k \mathbf{w} \cdot \mathbf{u} \, d\Omega + \int_{\Omega} \tilde{\boldsymbol{\varepsilon}}^e : \boldsymbol{\sigma} \, d\Omega + \int_{\Omega} \tilde{\boldsymbol{\varepsilon}}^p : \boldsymbol{\Sigma} \, d\Omega = \int_{\Gamma} \mathbf{w} \cdot (\boldsymbol{\sigma} \tilde{\mathbf{F}}^e + \boldsymbol{\Sigma} \tilde{\mathbf{F}}^p) \mathbf{n} \, d\Gamma \quad (45)$$

where $\Gamma := \partial\Omega$ is the boundary of Ω and \mathbf{n} is the unit normal to Γ . The symmetry of $\boldsymbol{\sigma}$ and $\boldsymbol{\Sigma}$ is used to obtain the last two integrals on the left-hand side, with

$$\tilde{\boldsymbol{\varepsilon}}^e := \frac{1}{2} \left[(\text{grad } \mathbf{w}) \tilde{\mathbf{F}}^e + \tilde{\mathbf{F}}^{eT} (\text{grad } \mathbf{w})^T \right], \quad \tilde{\boldsymbol{\varepsilon}}^p := \frac{1}{2} \left[(\text{grad } \mathbf{w}) \tilde{\mathbf{F}}^p + \tilde{\mathbf{F}}^{pT} (\text{grad } \mathbf{w})^T \right] \quad (46)$$

The weak form is first spatially discretised by interpolating \mathbf{u} and \mathbf{w} element-wise in terms of nodal quantities using appropriate nodal shape functions. This leads to a system of equations as in Eq. (20), but with the mass, damping and stiffness matrices given in terms of their IJ -th nodal submatrices as, respectively,

$$\mathbf{m}_{IJ}^e = \int_{\Omega^e} \rho f_m N_I N_J \, d\Omega \, \mathbf{I}, \quad \mathbf{c}_{IJ}^e = \int_{\Omega^e} \rho c_s f_c N_I N_J \, d\Omega \, \mathbf{I}, \quad \mathbf{k}_{IJ}^e = \int_{\Omega^e} \mu f_k N_I N_J \, d\Omega \, \mathbf{I} \quad (47a)$$

where N_I is the shape function for node I and \mathbf{I} is the identity matrix of size 2×2 . The element-level internal force term is given by

$$\mathbf{p}^e = \int_{\Omega^e} \tilde{\mathbf{B}}^{eT} \hat{\boldsymbol{\sigma}} \, d\Omega + \int_{\Omega^e} \tilde{\mathbf{B}}^{pT} \hat{\boldsymbol{\Sigma}} \, d\Omega \quad (47b)$$

where $\tilde{\mathbf{B}}^e$ and $\tilde{\mathbf{B}}^p$ are given in terms of their nodal submatrices as

$$\tilde{\mathbf{B}}_I^e := \begin{bmatrix} \tilde{N}_{I1}^e & \cdot \\ \cdot & \tilde{N}_{I2}^e \\ \tilde{N}_{I2}^e & \tilde{N}_{I1}^e \end{bmatrix}, \quad \tilde{\mathbf{B}}_I^p := \begin{bmatrix} \tilde{N}_{I1}^p & \cdot \\ \cdot & \tilde{N}_{I2}^p \\ \tilde{N}_{I2}^p & \tilde{N}_{I1}^p \end{bmatrix} \quad (48)$$

with

$$\tilde{N}_{Ii}^e := \tilde{F}_{ij}^e N_{I,j} \quad \text{and} \quad \tilde{N}_{Ii}^p := \tilde{F}_{ij}^p N_{I,j} \quad (49)$$

and

$$\hat{\boldsymbol{\sigma}} := \begin{Bmatrix} \sigma_{11} \\ \sigma_{22} \\ \sigma_{12} \end{Bmatrix} \quad (50)$$

with $\hat{\Sigma}$ the time-integral of $\hat{\sigma}$. The attenuation functions f_i^e and f_i^p are defined globally on the computational domain, not element-wise. It is conveniently assumed that there is no contribution to \mathbf{p}_{ext} from a free boundary of the PML.

Solution of the equations of motion [Eq. (20)] using a time-stepping algorithm requires calculating σ_{n+1} and Σ_{n+1} at t_{n+1} , to calculate \mathbf{p}_{n+1}^e , and also a consistent linearisation of \mathbf{p}_{n+1}^e at \mathbf{d}_{n+1} . Towards this, the approximations

$$\dot{\epsilon}(t_{n+1}) \approx \frac{\epsilon_{n+1} - \epsilon_n}{\Delta t}, \quad \mathbf{E}(t_{n+1}) \approx \mathbf{E}_n + \epsilon_{n+1} \Delta t \quad (51)$$

are used in Eq. (43c) to obtain

$$\hat{\epsilon}_{n+1} = \frac{1}{\Delta t} \left[\mathbf{B}^\epsilon \mathbf{v}_{n+1} + \mathbf{B}^\ell \mathbf{d}_{n+1} + \frac{1}{\Delta t} \hat{\mathbf{F}}^\epsilon \hat{\epsilon}_n - \hat{\mathbf{F}}^\ell \hat{\mathbf{E}}_n \right] \quad (52)$$

where

$$\hat{\epsilon} := \begin{Bmatrix} \epsilon_{11} \\ \epsilon_{22} \\ 2\epsilon_{12} \end{Bmatrix} \quad (53)$$

and $\hat{\mathbf{E}}$ is the time-integral of $\hat{\epsilon}$. The matrices \mathbf{B}^ϵ , \mathbf{B}^ℓ , $\hat{\mathbf{F}}^\epsilon$ and $\hat{\mathbf{F}}^\ell$ in Eq. (52) are defined in Appendix A.

The use of Eq. (51a) in the constitutive equation [Eq. (43b)] gives

$$\hat{\sigma}_{n+1} = \left(1 + \frac{2\zeta b}{c_s \Delta t} \right) \mathbf{D} \hat{\epsilon}_{n+1} - \frac{2\zeta b}{c_s \Delta t} \mathbf{D} \hat{\epsilon}_n \quad (54)$$

where

$$\mathbf{D} := \begin{bmatrix} \kappa + 4\mu/3 & \kappa - 2\mu/3 & \cdot \\ \kappa - 2\mu/3 & \kappa + 4\mu/3 & \cdot \\ \cdot & \cdot & \mu \end{bmatrix} \quad (55)$$

Furthermore, $\hat{\Sigma}_{n+1}$ is approximated as

$$\hat{\Sigma}_{n+1} = \hat{\Sigma}_n + \hat{\sigma}_{n+1} \Delta t \quad (56)$$

Substituting Eq. (56) into Eq. (47b) gives

$$\mathbf{p}_{n+1}^e = \int_{\Omega^e} \tilde{\mathbf{B}}^T \hat{\sigma}_{n+1} \, d\Omega + \int_{\Omega^e} \tilde{\mathbf{B}}^T \hat{\Sigma}_n \, d\Omega \quad (57)$$

where

$$\tilde{\mathbf{B}} := \tilde{\mathbf{B}}^e + \Delta t \tilde{\mathbf{B}}^p \quad (58)$$

Linearisation of Eq. (57) gives, on using Eq. (54) alongwith Eq. (52),

$$\Delta \mathbf{p}_{n+1}^e = \left[\int_{\Omega^e} \tilde{\mathbf{B}}^T \tilde{\mathbf{D}} \mathbf{B}^\epsilon \, d\Omega \right] \Delta \mathbf{v}_{n+1} + \left[\int_{\Omega^e} \tilde{\mathbf{B}}^T \tilde{\mathbf{D}} \mathbf{B}^\ell \, d\Omega \right] \Delta \mathbf{d}_{n+1} \quad (59)$$

where

$$\tilde{\mathbf{D}} = \frac{1}{\Delta t} \left(1 + \frac{2\zeta b}{c_s \Delta t} \right) \mathbf{D} \quad (60)$$

i.e., this linearisation gives tangent matrices

$$\check{\mathbf{c}}^e := \int_{\Omega^e} \tilde{\mathbf{B}}^T \tilde{\mathbf{D}} \mathbf{B}^e \, d\Omega, \quad \check{\mathbf{k}}^e := \int_{\Omega^e} \tilde{\mathbf{B}}^T \tilde{\mathbf{D}} \mathbf{B}^e \, d\Omega \quad (61)$$

which may be incorporated into the effective tangent stiffness used in the time-stepping algorithm. Unfortunately, these matrices are not symmetric. However, since all the system matrices are independent of \mathbf{d} , this is effectively a linear model. Note that the attenuation functions, representing the coordinate-stretching, affect the various compatibility matrices, e.g., $\tilde{\mathbf{B}}^e$, $\tilde{\mathbf{B}}^e$ etc. but not the material moduli matrix \mathbf{D} . Consequently, this plane-strain FE formulation can be applied to plane-stress problems by re-defining κ appropriately.

The profusion of notation and equations in this section cries out for a synopsis of the algorithm for computing the element-level effective internal force and tangent stiffness; this is presented in Box II.

3.5. Numerical results

Numerical results are presented for the classical soil-structure interaction problems of a rigid strip-footing on a i) half-plane, ii) layer on a half-plane, and iii) layer on a rigid base.

Figure 7(a) shows a cross section of a rigid strip-footing of half-width b with its three degrees-of-freedom (DOFs) identified — vertical (V), horizontal (H), and rocking (R) — supported by a homogeneous isotropic (visco-)elastic half-plane with shear modulus μ , mass density ρ , Poisson's ratio ν , and Voigt damping ratio ζ for the visco-elastic medium. The time-domain response of this system is studied through the reactions along the three DOFs due to an imposed displacement along any of the three DOFs; the imposed displacement is chosen to be of the form of Eq. (33) and the reaction along DOF i due to an imposed displacement along j is denoted by P_{ij} , with $i, j \in \{V, H, R\}$.

This unbounded-domain system is modelled using the bounded-domain-PML model shown in Fig. 7(b), composed of a bounded domain Ω_{BD} and a PML Ω_{PM} , with the attenuation functions in Eq. (12) chosen as $f_i^e = f_i^p = f_i$, with f_i chosen to be linear in the PML. A finite element mesh of four-node bilinear isoparametric elements are used to discretise the entire bounded domain. The mesh chosen is reasonably dense and is graded to capture sharp variations in stresses near the footing. For comparison, the half-plane is also modelled using a viscous-dashpot model [3], wherein the entire domain $\Omega_{\text{BD}} \cup \Omega_{\text{PM}}$ is taken to be (visco-)elastic and consistent dashpot elements replace the fixed outer boundary; thus the mesh used for the dashpot model is comparable to that used for the PML model. Because of the dearth of analytical results in the time domain, the half-plane is modelled using an extended mesh; the results from this mesh will serve as a benchmark. From the center of the footing,

Box II. Computing effective force and stiffness for plane-strain PML element.

1. Compute system matrices \mathbf{m}^e , \mathbf{c}^e and \mathbf{k}^e [Eq. (47a)].
2. Compute internal force \mathbf{p}_{n+1}^e [Eq. (57)]. Use $\hat{\boldsymbol{\varepsilon}}_{n+1}$ [Eq. (52)] and $\hat{\boldsymbol{\sigma}}_{n+1}$ [Eq. (54)].
3. Compute tangent matrices $\check{\mathbf{c}}^e$ and $\check{\mathbf{k}}^e$ [Eq. (61)].
4. Compute effective internal force $\tilde{\mathbf{p}}_{n+1}^e$ and tangent stiffness $\tilde{\mathbf{k}}^e$:

$$\begin{aligned}\tilde{\mathbf{p}}_{n+1}^e &= \mathbf{m}^e \mathbf{a}_{n+1} + \mathbf{c}^e \mathbf{v}_{n+1} + \mathbf{k}^e \mathbf{d}_{n+1} + \mathbf{p}_{n+1}^e \\ \tilde{\mathbf{k}}^e &= \alpha_k (\mathbf{k}^e + \check{\mathbf{k}}^e) + \alpha_c (\mathbf{c}^e + \check{\mathbf{c}}^e) + \alpha_m \mathbf{m}^e\end{aligned}$$

where $\mathbf{a}_{n+1} \approx \ddot{\mathbf{d}}(t_{n+1})$, and, for example,

$$\alpha_k = 1, \quad \alpha_c = \frac{\gamma}{\beta \Delta t}, \quad \alpha_m = \frac{1}{\beta \Delta t^2}$$

for the Newmark method.

Note: The tangent stiffness $\tilde{\mathbf{k}}^e$ is independent of the solution, and thus has to be computed only once. However, the internal force \mathbf{p}_{n+1}^e has to be re-computed at each time-step because it is dependent on the solution at past times.

this mesh extends to a distance of $10b$ downwards and laterally; the entire domain is taken to be (visco-)elastic, and viscous dashpots are placed on the outer boundary.

Figure 8(a) compares the reactions computed for an elastic medium using the PML model and the dashpot model with results from the extended mesh. Note that the bounded domain for the PML and the dashpot models is small, extending only upto $b/2$ on either side of the footing and below it, and the PML width equal to b , the half-width of the footing. The results obtained from the PML model follow the extended mesh results closely, even though the domain is small enough for the dashpots to reflect waves back to the footing within the time-interval considered. Although the computational cost of the PML model is approximately twice that of the dashpot model, this cost is not significantly large because the dashpot model itself is computationally inexpensive. Thus, the highly accurate results from the PML model are obtained at low computational cost. The small-scale oscillations in the results are presumably due to numerical reflections from the mesh. Figure 8(b) presents similar comparisons for a visco-elastic half-plane. The PML results are visually indistinguishable from the extended mesh results, even though the computational domain

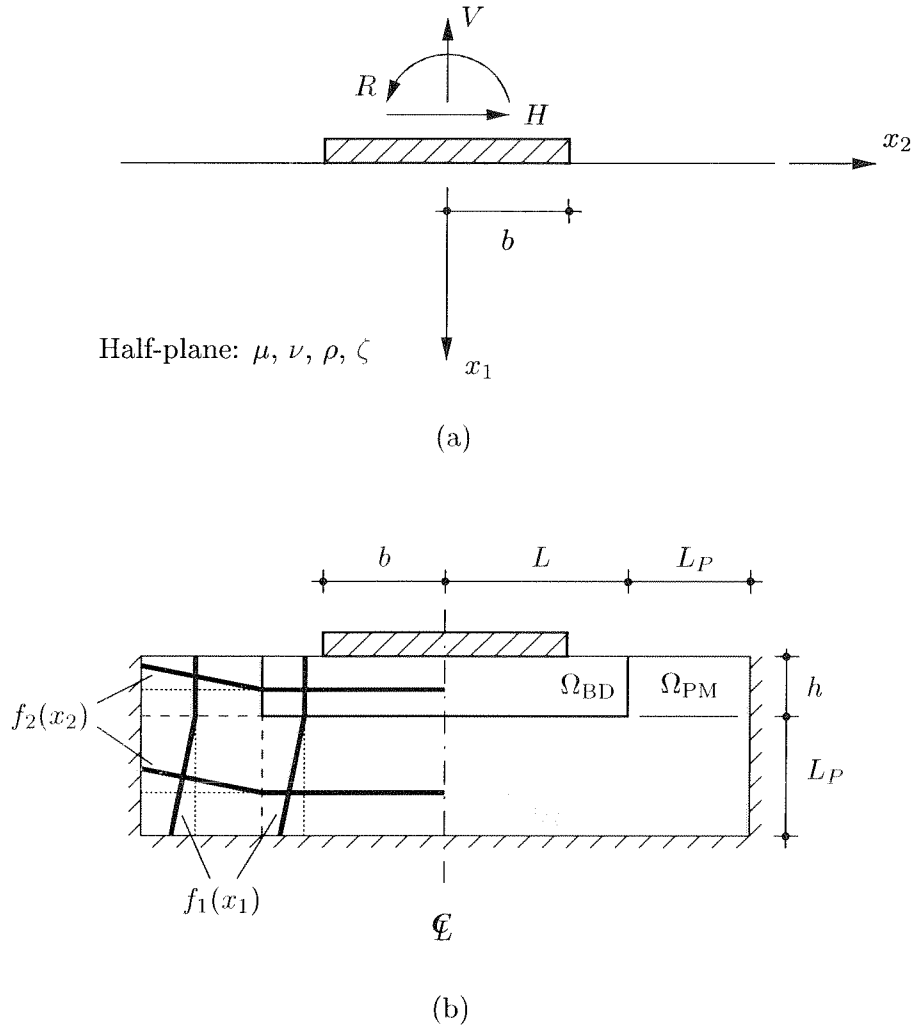


Figure 7. (a) Cross-section of a rigid strip of half-width b on a homogeneous isotropic (visco-)elastic half-plane; (b) a PML model.

is small: the dashpots generate spurious reflections even when the medium is visco-elastic. Not surprisingly, the small numerical oscillations — observed in the results for the elastic half-plane — disappear when material damping is incorporated into the medium.

Figures 9 and 10 present frequency-dependent flexibility coefficients $F_{ij}(a_0)$ for the rigid strip-footing on a half-plane computed using a PML model employing the time-domain stretching functions in Eq. (12). The flexibility coefficients are defined as the displacement amplitudes along DOF i due to a unit-amplitude harmonic force along DOF j . Results for the elastic half-plane are compared in Fig. 9 against available analytical results [40]. Due to the dearth of analytical solutions for the strip on a Voigt visco-elastic half-plane, the results

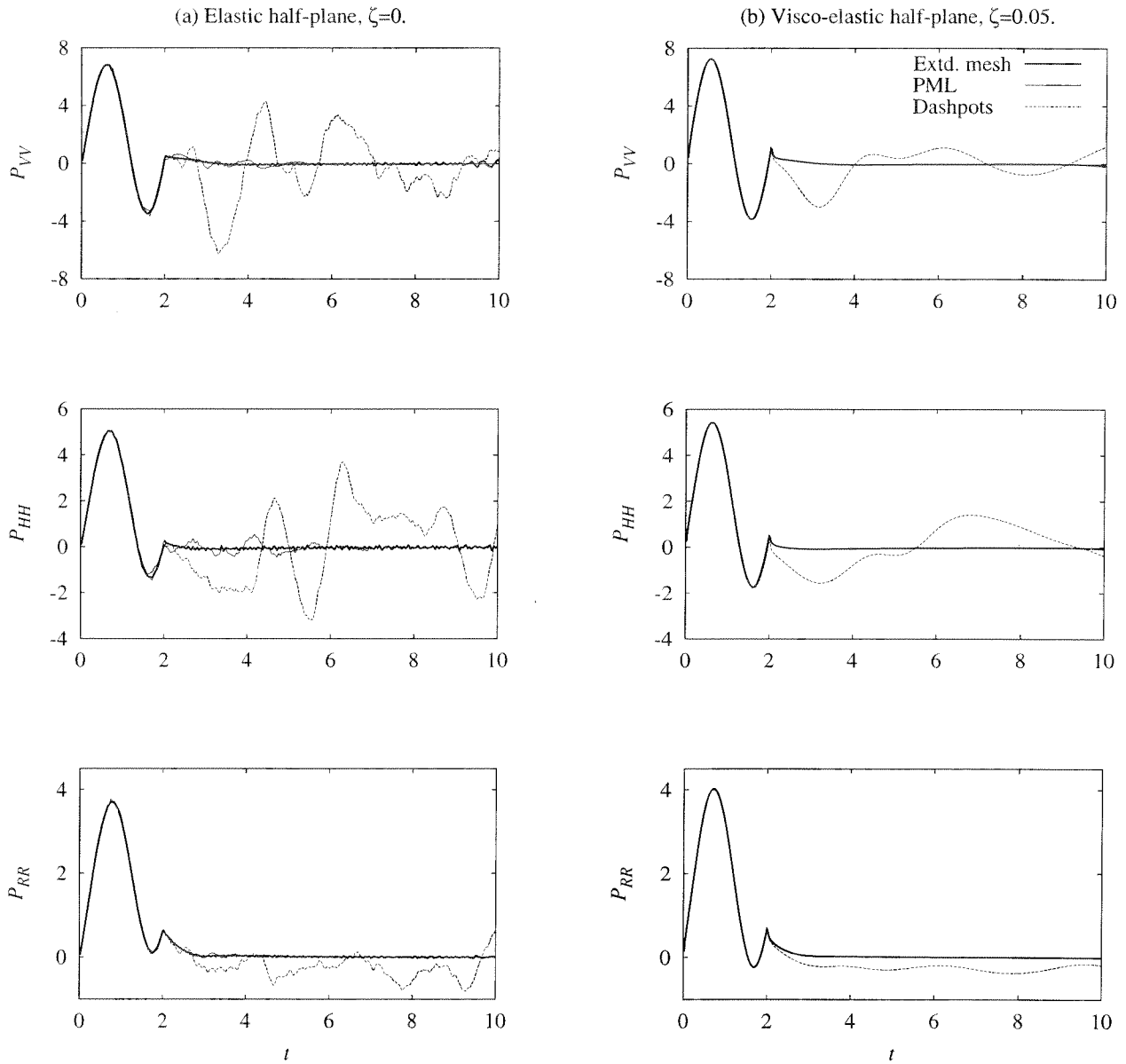


Figure 8. Reactions of a rigid strip on (visco-)elastic half-plane due to imposed displacements; $L = 3b/2$, $h = b/2$, $L_P = b$, $f_1(x_1) = 10\langle x_1 - h \rangle / L_P$, $f_2(x_2) = 10\langle |x_2| - L \rangle / L_P$; $t_d = 2$, $\Delta t = 0.02$; $\langle x \rangle := (x + |x|)/2$; $\mu = 1$, $\nu = 0.25$.

obtained from the (possibly less accurate) time-domain stretching functions are compared in Fig. 10 to results from a PML model employing the frequency-domain-only stretching functions [Eq. (34)], denoted by “FD PML” in the figures. The rationale behind this approach is that the frequency-domain stretching functions produce highly accurate results for hysteretic damping [30] and, hence, can be expected to also produce excellent results for Voigt damping. The results demonstrate that the time-domain stretching functions indeed produce accurate results as expected, because the wave motion in the half-plane consists primarily of propagating modes, which are adequately attenuated even by the time-domain stretching functions.

Figure 11(a) shows a cross section of the rigid strip supported by a layer on a half-plane, and Fig. 11(b) shows a corresponding PML model with the attenuation functions in Eq. (12) chosen as $f_i^e = f_i^p = f_i$, with f_i chosen to be linear in the PML. The elastic moduli for the PMLs employed for the layer and the half-plane are set to the moduli for the corresponding elastic media. For comparison, a viscous-dashpot model is also employed, where the entire bounded domain is taken to be (visco-)elastic and consistent dashpots replace the fixed outer boundary. An extended-mesh model, with viscous dashpots at the outer boundary, is taken as a benchmark model for the layer on a half-plane; this mesh extends to a distance of $10b$ laterally and downwards from the center of the footing.

Figure 12 shows the reactions of the rigid strip on a layer-on-half-plane due to imposed displacements. The PML results typically follow the results from the extended mesh, even though the domain is small enough for the viscous dashpots to generate considerable spurious reflections. The computational cost of the PML model is not significantly large: it is approximately twice that of the dashpot model. Significantly, the extended-mesh results show spurious reflections for vertical motion of the footing: the P-wave speed in the half-plane is high enough that the depth of the extended mesh is not adequate for the time interval in the analysis. Figures 13 and 14 demonstrate that the time-domain stretching functions provide frequency-dependent flexibility coefficients that closely match those obtained using the frequency-domain-only stretching functions.

Figure 15(a) shows a cross section of the rigid strip supported by a layer on a rigid base, and Fig. 15(b) shows a corresponding PML model where $f_i^e = f_i^p = f_i$ in Eq. (12), with $f_1(x_1) = 0$ and $f_2(x_2)$ linear in the PML. The corresponding viscous-dashpot model includes the entire bounded domain as (visco-)elastic, with viscous dashpots replacing the fixed lateral boundaries. The extended-mesh model is also a viscous-dashpot model, but extending to $10b$ on either side from the center of the footing. Figure 16 demonstrates the high accuracy of the PML model, as well as the small size of the computational domain through the inadequacy of the dashpot model. These results from the PML model are obtained at a cost approximately twice that of the dashpot model, i.e., the computational cost is not significantly large.

Figure 17 demonstrates that for a rigid strip on an elastic layer on rigid base, the frequency-dependent flexibility coefficients obtained using the time-domain stretching functions do not always closely follow those from the frequency-domain only stretching functions; this is presumably due to the presence of evanescent modes in the system. This apparent in-

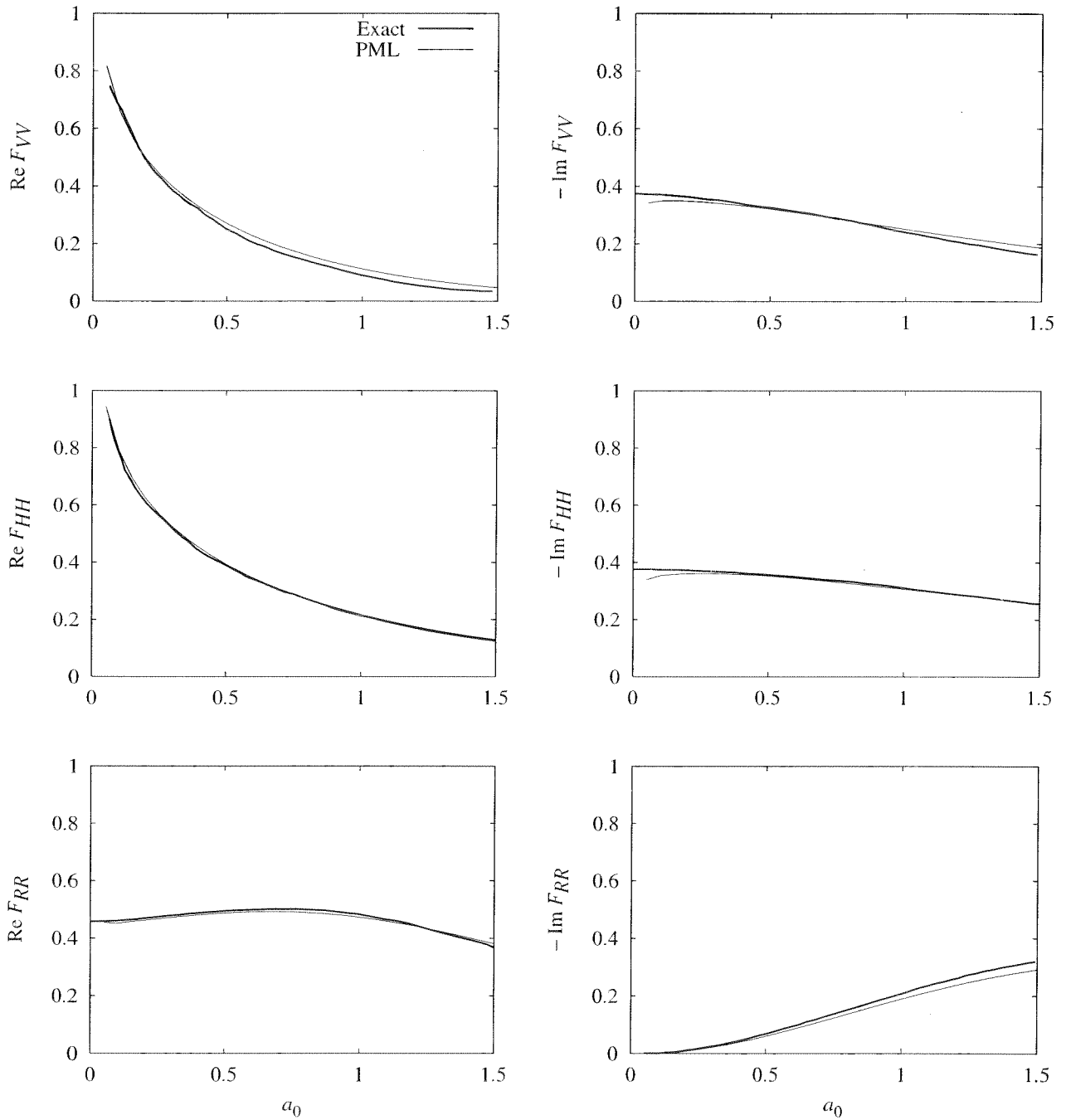


Figure 9. Dynamic flexibility coefficients of rigid strip on elastic half-plane computed using a PML model with stretching functions suitable for time-domain analysis; $L = 3b/2$, $h = b/2$, $L_P = b$, $f_1(x_1) = 10\langle x_1 - h \rangle / L_P$, $f_2(x_2) = 10\langle |x_2| - L \rangle / L_P$; $\mu = 1$, $\nu = 0.25$; “Exact” results from Ref. 40.

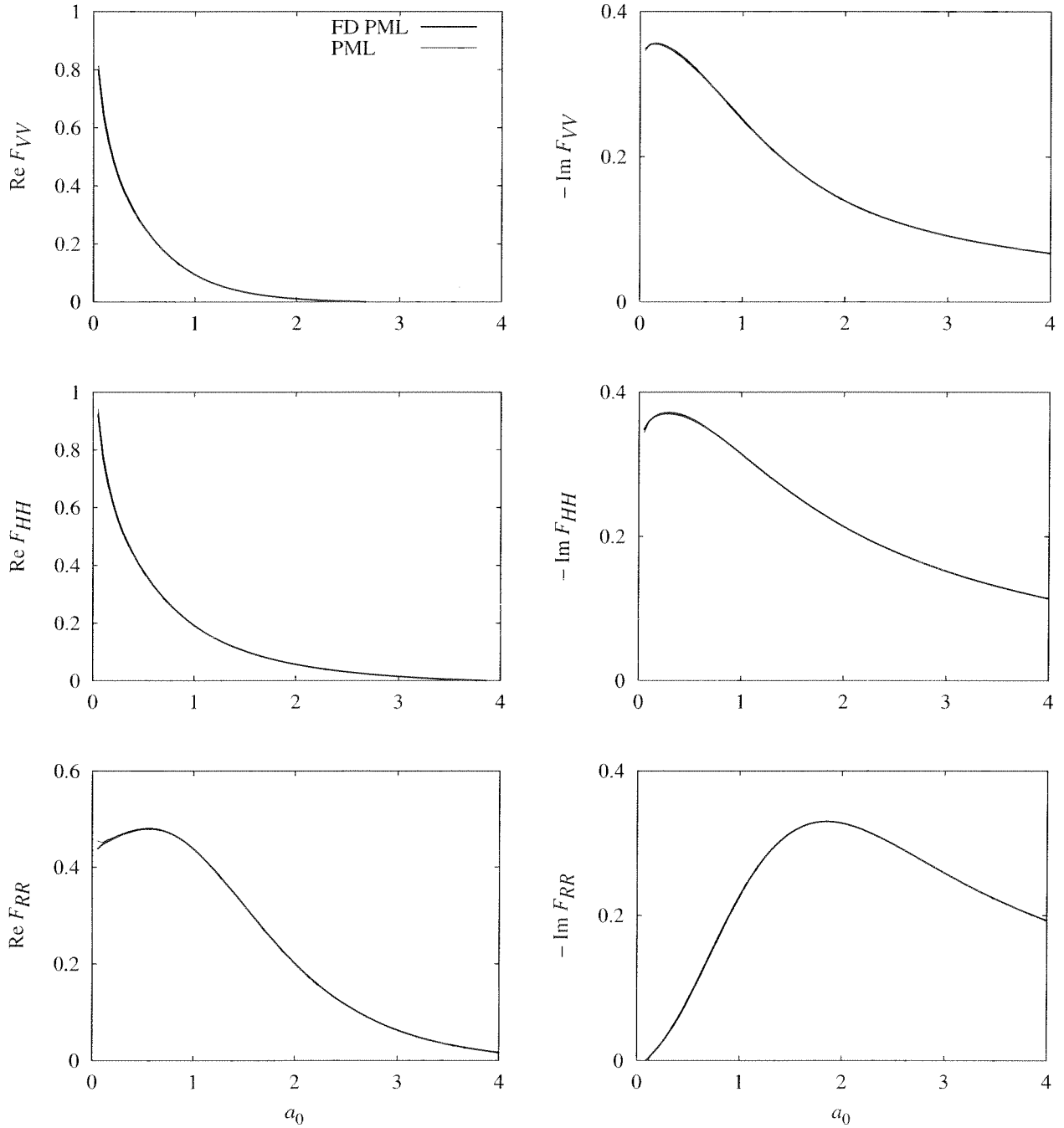


Figure 10. Dynamic flexibility coefficients of rigid strip on visco-elastic half-plane computed using a PML model with stretching functions suitable for time-domain analysis; $L = 3b/2$, $h = b/2$, $L_P = b$, $f_1(x_1) = 10\langle x_1 - h \rangle / L_P$, $f_2(x_2) = 10\langle |x_2| - L \rangle / L_P$; $\mu = 1$, $\nu = 0.25$, $\zeta = 0.05$; “FD PML”: a substitute for an exact result, obtained using frequency-domain stretching functions in PML model.

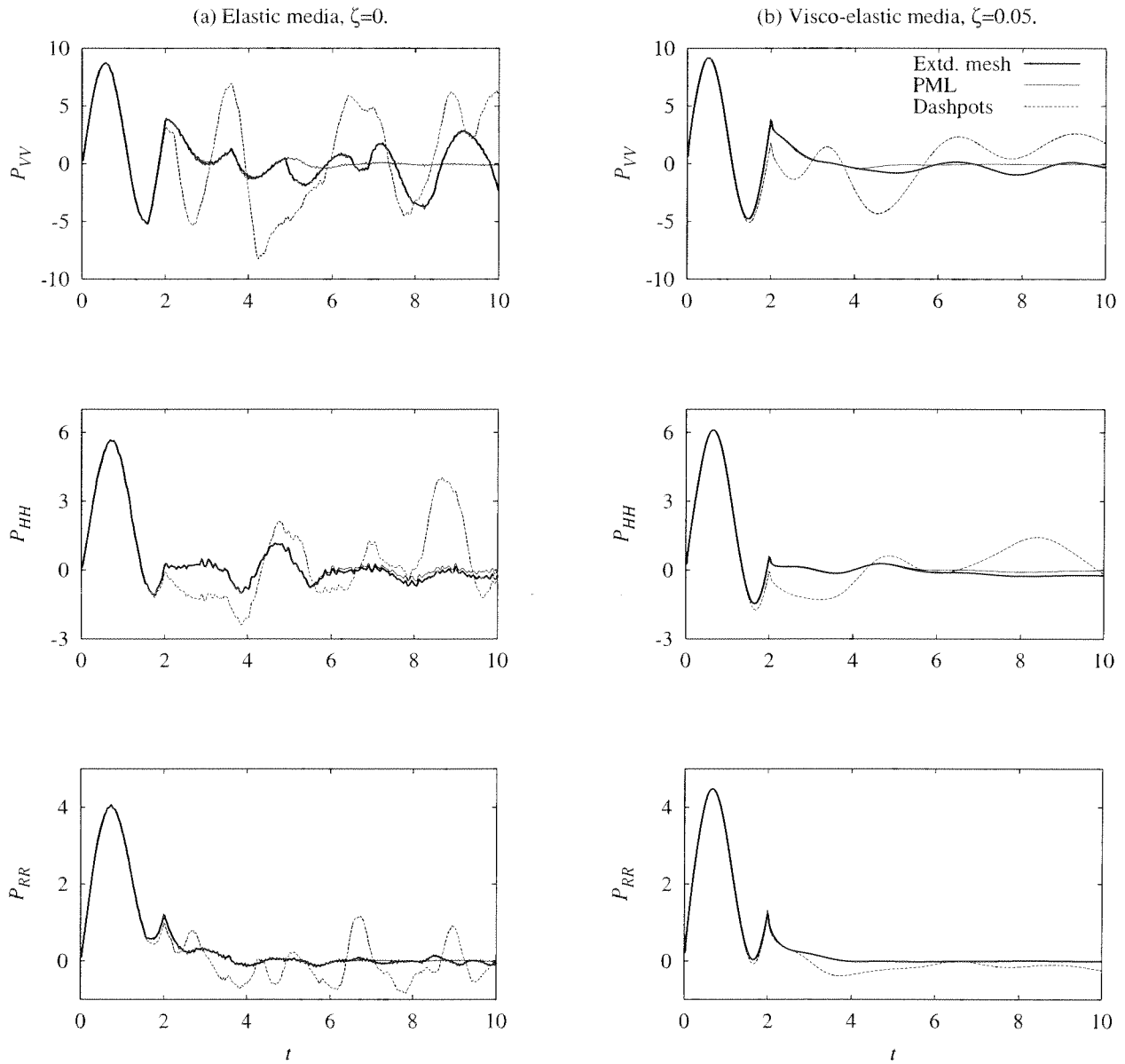


Figure 12. Reactions of a rigid strip on (visco-)elastic layer on half-plane, due to imposed displacements; $L = 3b/2$, $L_P = b$, $h = b/2$, $f_1(x_1) = 10\langle x_1 - (d + h) \rangle / L_P$, $f_2(x_2) = 10\langle |x_2| - L \rangle / L_P$; $t_d = 2$, $\Delta t = 0.02$; $d = 2b$, $\mu_l = 1$, $\mu_h = 4\mu_l$, $\nu = 0.4$.

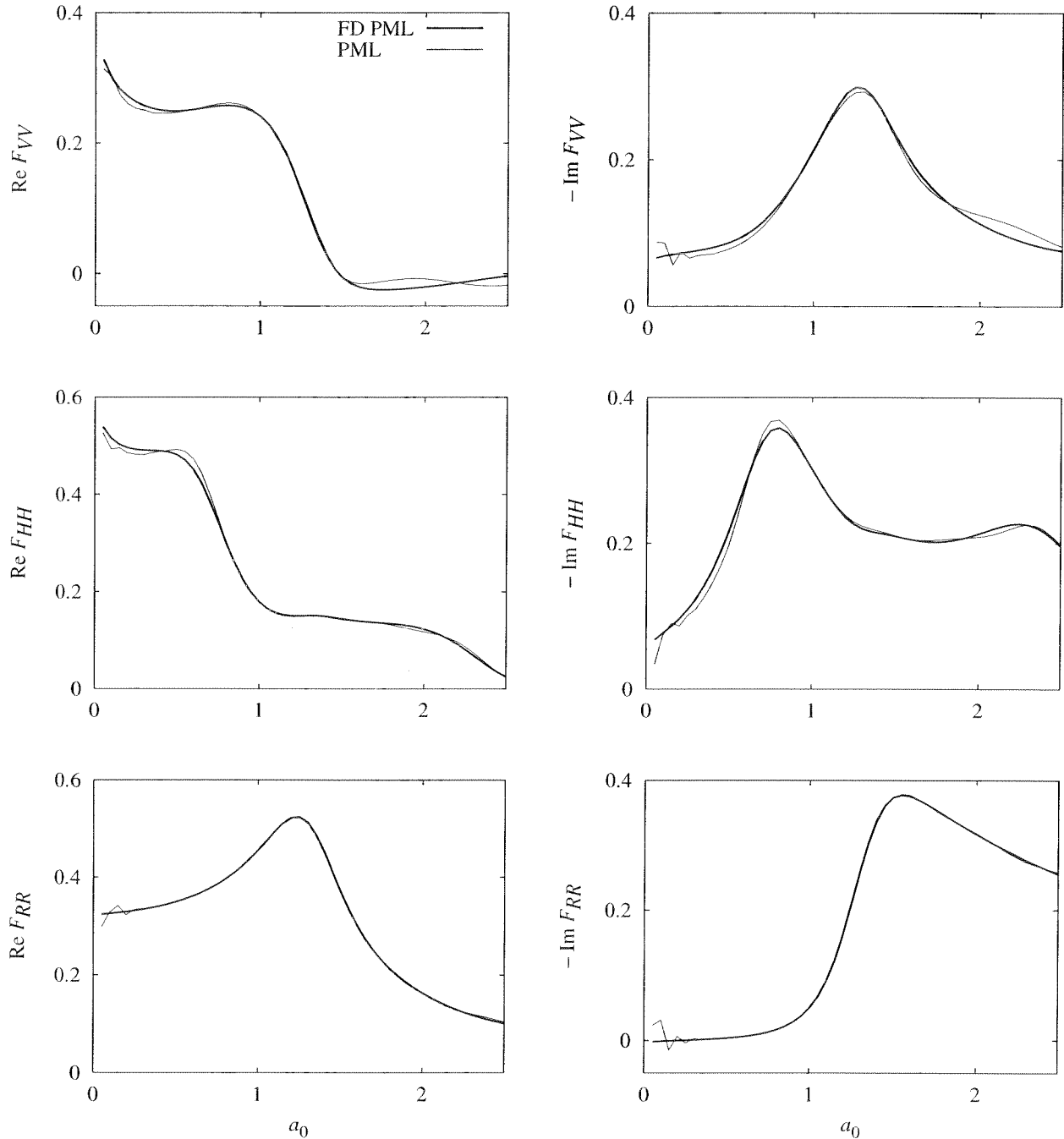


Figure 13. Dynamic flexibility coefficients of rigid strip on elastic layer on half-plane computed using a PML model with stretching functions suitable for time-domain analysis; $L = 3b/2$, $L_P = b$, $h = b/2$, $f_1(x_1) = 10\langle x_1 - (d + h) \rangle / L_P$, $f_2(x_2) = 10\langle |x_2| - L \rangle / L_P$; $d = 2b$, $\mu_l = 1$, $\mu_h = 4\mu_l$, $\nu = 0.4$, $a_0 = \omega b / \sqrt{\mu_l / \rho}$; “FD PML”: a substitute for an exact result, obtained using frequency-domain stretching functions in PML model.

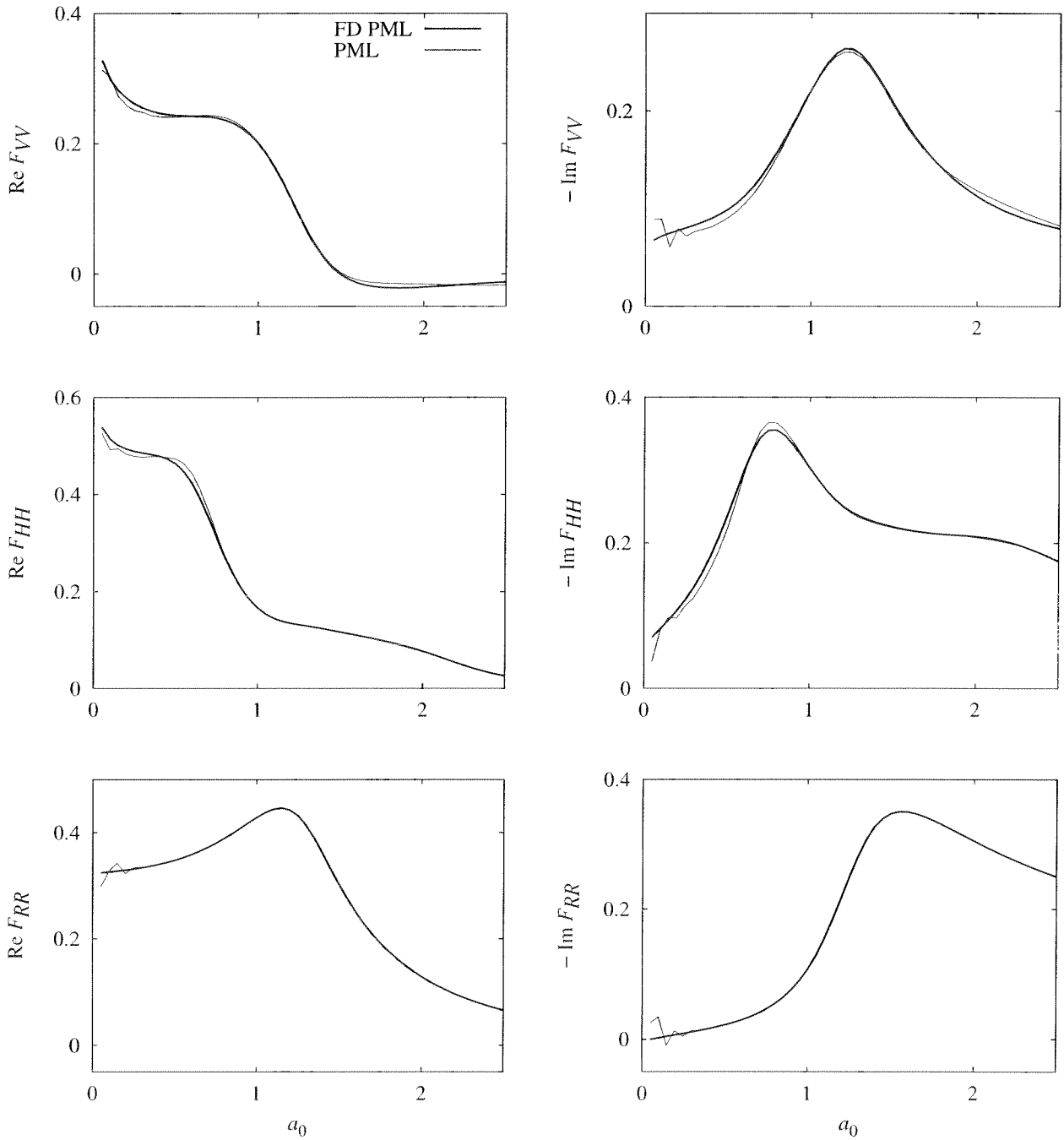


Figure 14. Dynamic flexibility coefficients of rigid strip on visco-elastic layer on half-plane computed using a PML model with stretching functions suitable for time-domain analysis; $L = 3b/2$, $L_P = b$, $h = b/2$, $f_1(x_1) = 10\langle x_1 - (d+h) \rangle / L_P$, $f_2(x_2) = 10\langle |x_2| - L \rangle / L_P$; $d = 2b$, $\mu_l = 1$, $\mu_h = 4\mu_l$, $\nu = 0.4$, $\zeta = 0.05$, $a_0 = \omega b / \sqrt{\mu_l / \rho}$; “FD PML”: a substitute for an exact result, obtained using frequency-domain stretching functions in PML model.

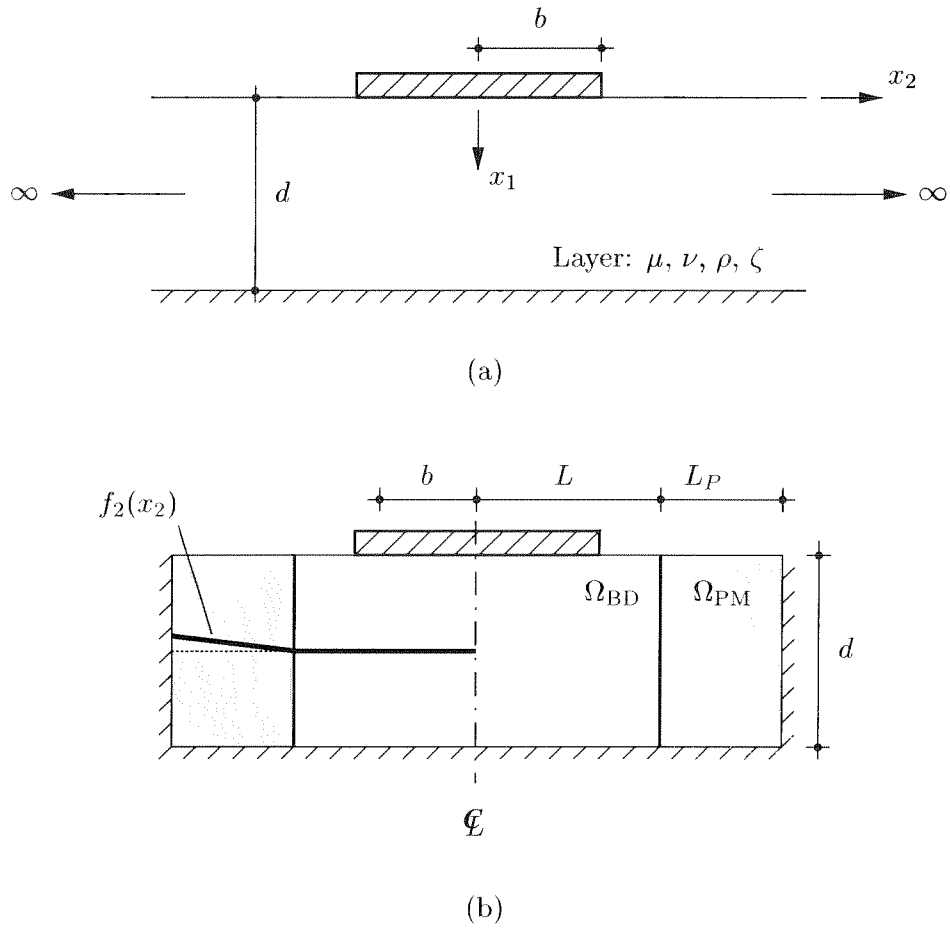


Figure 15. (a) Cross-section of the rigid strip of half-width b on a homogeneous isotropic (visco-)elastic layer on rigid base; (b) a PML model.

domain response is the superposition of time-harmonic responses over a range of frequencies, and because the energy of the excitation in this frequency-band is small compared to its energy in the rest of the spectrum, inaccuracies in this band do not affect the overall accuracy of the response. The time-domain stretching functions provide accurate results for a rigid strip on a visco-elastic layer, as demonstrated in Fig. 18.

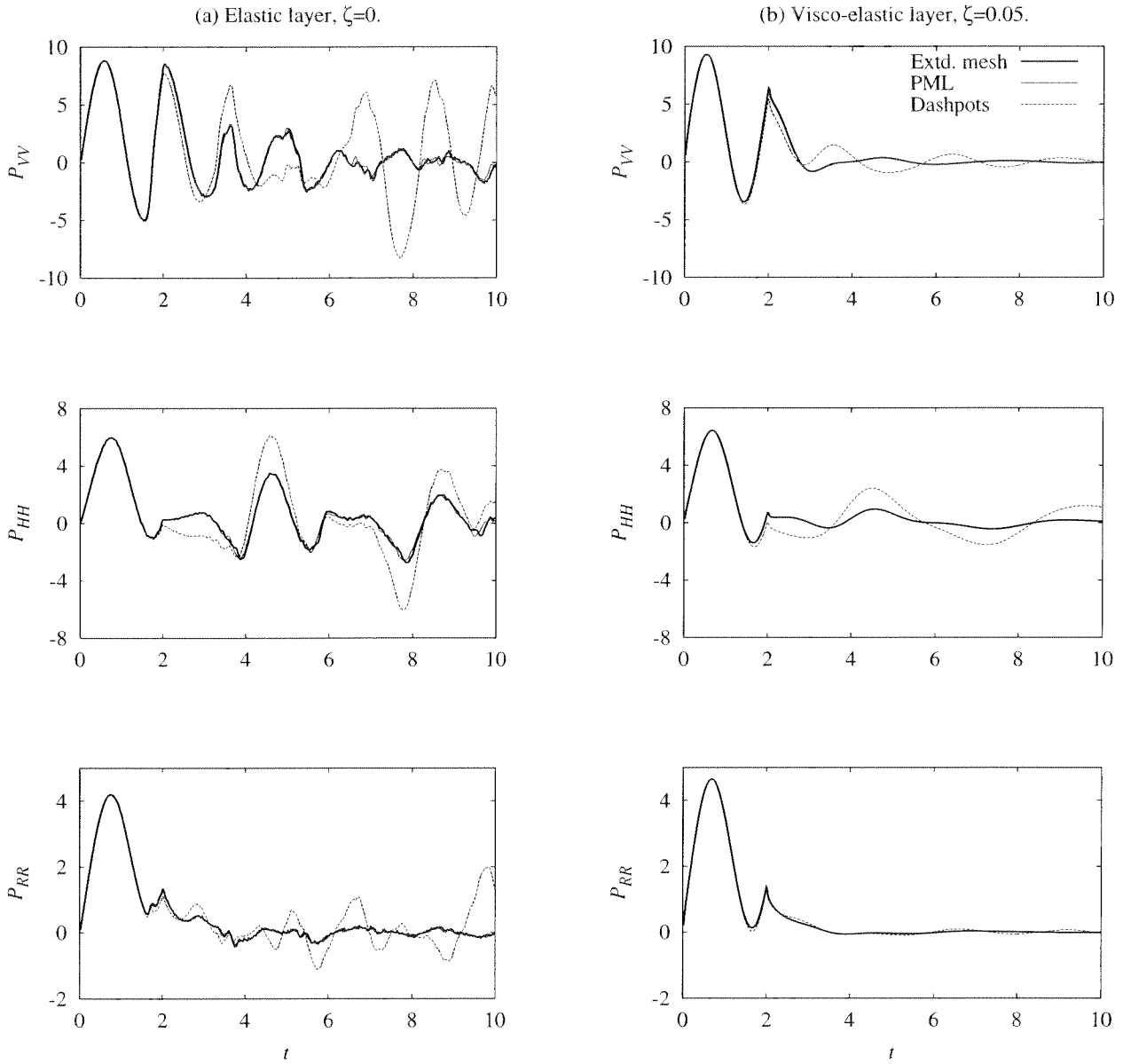


Figure 16. Reactions of a rigid strip on (visco-)elastic layer on rigid base, due to imposed displacements; $L = 3b/2$, $L_P = b$, $f_1(x_1) = 0$, $f_2(x_2) = 20(|x_2| - L)/L_P$; $t_d = 2$, $\Delta t = 0.02$; $d = 2b$, $\mu = 1$, $\nu = 0.4$.

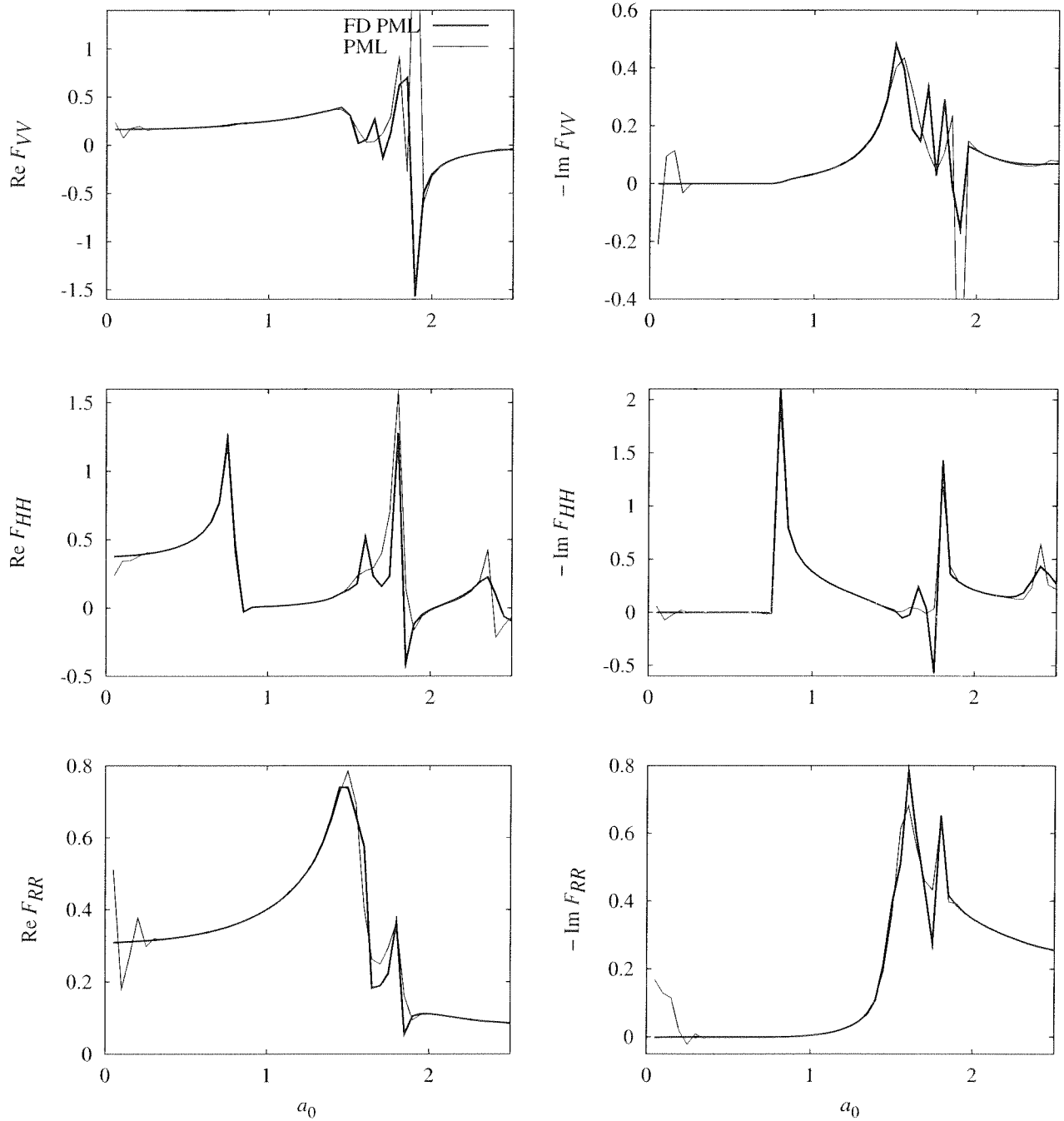


Figure 17. Dynamic flexibility coefficients of rigid strip on elastic layer on rigid base computed using a PML model with stretching functions suitable for time-domain analysis; $L = 3b/2$, $L_P = b$, $f_1(x_1) = 0$, $f_2(x_2) = 20(|x_2| - L)/L_P$; $d = 2b$, $\mu = 1$, $\nu = 0.4$; “FD PML”: a substitute for an exact result, obtained using frequency-domain stretching functions in PML model.

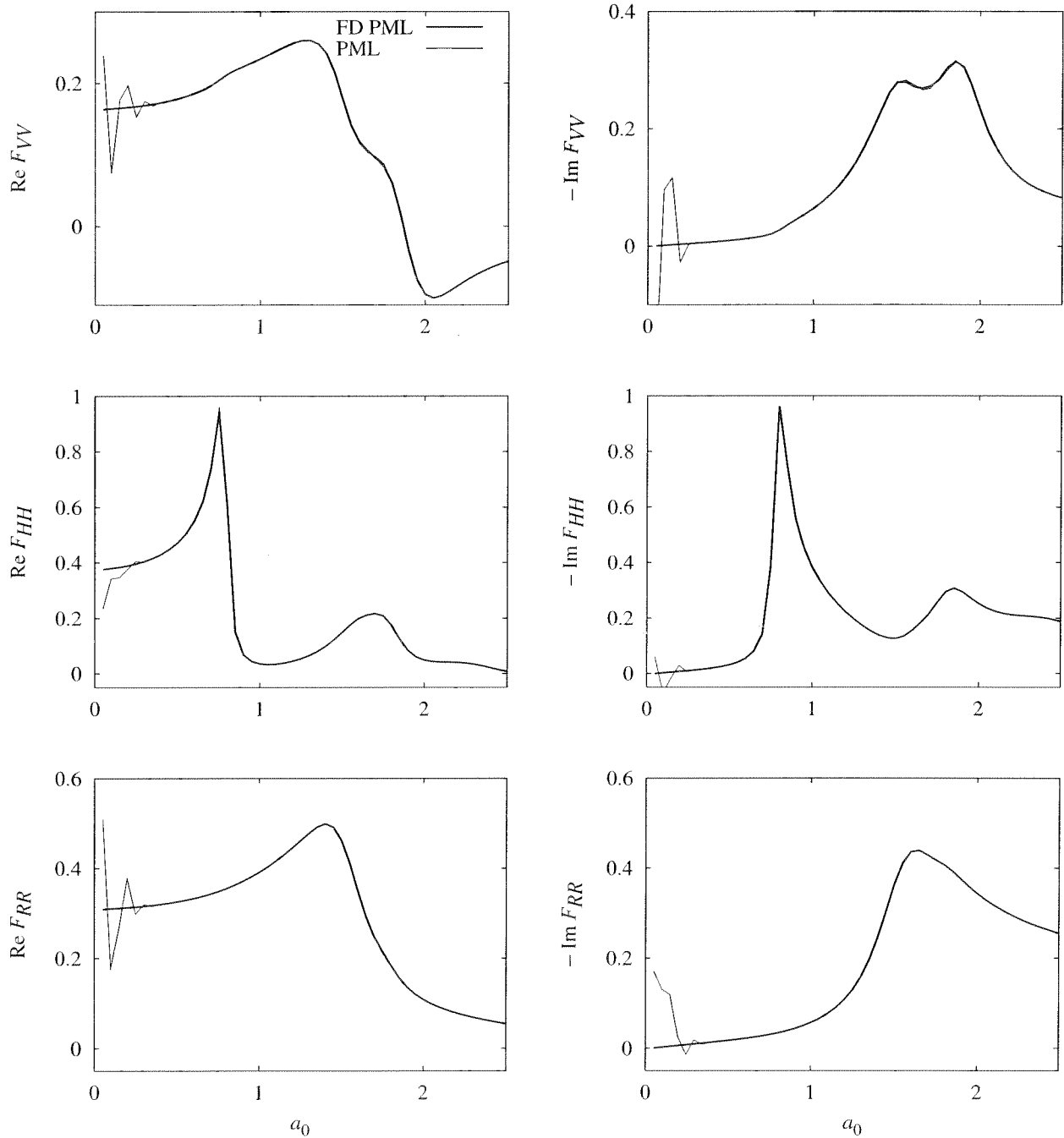


Figure 18. Dynamic flexibility coefficients of rigid strip on visco-elastic layer on rigid base computed using a PML model with stretching functions suitable for time-domain analysis; $L = 3b/2$, $L_P = b$, $f_1(x_1) = 0$, $f_2(x_2) = 20(|x_2| - L)/L_P$; $d = 2b$, $\mu = 1$, $\nu = 0.4$, $\zeta = 0.05$; “FD PML”: a substitute for an exact result, obtained using frequency-domain stretching functions in PML model.

4. CONCLUSIONS

Building on recent formulations for corresponding time-harmonic PMLs [30], this paper has presented displacement-based, time-domain equations for the PMLs for anti-plane and for plane-strain motion of a two-dimensional (visco-)elastic continuum. These equations are obtained by selecting stretching functions in the PML that have a simple dependence on the factor $i\omega$, which facilitates transformation of the time-harmonic equations into the time domain. In the interest of obtaining a realistic model of the unbounded domain, material damping is introduced into the PML equations in the form of a Voigt damping model in the constitutive relation for the PML; this model is chosen instead of the traditional hysteretic damping model because the latter is non-causal.

These PML equations have been implemented numerically by a straightforward finite-element approach. As is conventional, the “equilibrium” equations are discretised in time by a traditional integrator, such as the Newmark method; the equilibrium equations are solved at each time-station using a Newton-Raphson iteration scheme. Because, the tangent stiffness matrix employed in the Newton-Raphson scheme is independent of the solution, it is computed only once at the start of the analysis. Moreover, because the tangent is independent of the solution, the PML model is effectively a linear model. The tangent stiffness of the anti-plane PML is found to be symmetric. Furthermore, it is argued that if the attenuation functions are positive-valued, and if the boundary restraints on the whole domain are adequate, then the tangent stiffness of the entire computational domain will be positive definite. Unfortunately, the tangent stiffness of the plane-strain PML turns out to be unsymmetric.

These FE implementations of the PMLs are employed to solve the canonical problem of the anti-plane motion of a semi-infinite layer on a rigid base and the classical soil-structure interaction problems of a rigid strip-footing on a i) half-plane, ii) layer on a half-plane, and iii) layer on a rigid base. Highly accurate results were obtained from PML models with small bounded domains at low computational costs. The bounded domains employed for these problems were small enough that comparable viscous-dashpot models generated significant spurious reflections within the time-interval of the analysis, even if the domain was visco-elastic. The computational costs of the PML models were not significantly large: the cost of the anti-plane PML models was only slightly larger than that of the corresponding dashpot models, and the cost of the plane-strain PML models was approximately twice that of the dashpot models.

Frequency-domain results suggest that the time-domain results may not be accurate for an elastic system if the excitation is primarily in a frequency-band where evanescent modes are predominant. If the excitation is broadband, however, and evanescent modes are dominant only in a narrow frequency-band, then the time-domain results can be expected to be accurate. Moreover, the results are accurate for a visco-elastic system because the evanescent modes are attenuated by damping. Issues about inaccuracies due to evanescent modes are of concern primarily in waveguide systems — such as the layer on a rigid base — because of

their severely-constricted geometries; evanescent modes are of less concern in half-plane or full-plane problems. Note that this issue arises in the time-domain model of the PML because the special choice of stretching functions does not always adequately attenuate evanescent modes. An alternate choice of the stretching function for a frequency-domain PML model produces accurate results even for waveguide systems with significant evanescent modes [30]; however, it is difficult to employ such a frequency-domain stretching function in a direct time-domain analysis.

This paper presented time-domain PML models for isotropic, homogeneous or discretely-inhomogeneous media only. However, the constitutive relation for the PML is the same as that for the elastic medium. This suggests that the PML formulations presented in this paper may be extended to anisotropic, continuously-inhomogeneous elastic media with at most minimal modifications, mirroring similar developments in electromagnetics [41].

ACKNOWLEDGEMENTS

The authors are grateful to Prof. Robert L. Taylor, Prashanth K. Vijalapura and Prof. Fernando L. Teixeira for their helpful advice and comments.

APPENDIX A

The matrices \mathbf{B}^ϵ , \mathbf{B}^ϱ , $\hat{\mathbf{F}}^\epsilon$ and $\hat{\mathbf{F}}^\varrho$ used in Eq. (52) in Sec. 3.4 are defined as follows. Define

$$\mathbf{F}^\varrho := \left[\frac{\mathbf{F}^e}{\Delta t} + \mathbf{F}^p \right]^{-1}, \quad \mathbf{F}^\epsilon := \mathbf{F}^e \mathbf{F}^\varrho, \quad \mathbf{F}^\varrho := \mathbf{F}^p \mathbf{F}^\epsilon \quad (\text{A1})$$

Then \mathbf{B}^ϵ is defined in terms of nodal submatrices as

$$\mathbf{B}_I^\epsilon := \begin{bmatrix} F_{11}^\epsilon N_{I1}^\varrho & F_{21}^\epsilon N_{I1}^\varrho \\ F_{12}^\epsilon N_{I2}^\varrho & F_{22}^\epsilon N_{I2}^\varrho \\ F_{11}^\epsilon N_{I2}^\varrho + F_{12}^\epsilon N_{I1}^\varrho & F_{21}^\epsilon N_{I2}^\varrho + F_{22}^\epsilon N_{I1}^\varrho \end{bmatrix} \quad (\text{A2})$$

where

$$N_{Ii}^\varrho := F_{ij}^\varrho N_{I,j} \quad (\text{A3})$$

The matrix \mathbf{B}^ϱ is defined similarly, with \mathbf{F}^ϱ replacing \mathbf{F}^ϵ throughout. Furthermore,

$$\hat{\mathbf{F}}^\epsilon := \begin{bmatrix} F_{11}^{\epsilon 2} & F_{21}^{\epsilon 2} & F_{11}^\epsilon F_{21}^\epsilon \\ F_{12}^{\epsilon 2} & F_{22}^{\epsilon 2} & F_{12}^\epsilon F_{22}^\epsilon \\ 2F_{11}^\epsilon F_{12}^\epsilon & 2F_{21}^\epsilon F_{22}^\epsilon & F_{11}^\epsilon F_{22}^\epsilon + F_{12}^\epsilon F_{21}^\epsilon \end{bmatrix} \quad (\text{A4})$$

and $\hat{\mathbf{F}}^\varrho$ is defined similarly, with \mathbf{F}^ϱ replacing \mathbf{F}^ϵ throughout.

REFERENCES

1. Wolf JP. *Soil-Structure-Interaction Analysis in Time Domain*. Prentice-Hall: Englewood Cliffs, NJ, 1988.
2. Bao H, Bielak J, Ghattas O, Kallivokas LF, O'Hallaron DR, Shewchuck JR, Xu J. Large-scale simulation of elastic wave propagation in heterogeneous media on parallel computers. *Computer Methods in Applied Mechanics and Engineering* 1998; **152**(1-2):85-102.
3. Lysmer J, Kuhlemeyer RL. Finite dynamic model for infinite media. *Journal of the Engineering Mechanics Division, ASCE* 1969; **95**(EM4):859-877.
4. Clayton R, Engquist B. Absorbing boundary conditions for acoustic and elastic wave equations. *Bulletin of the Seismological Society of America* 1977; **67**(6):1529-1540.
5. Higdon RL. Absorbing boundary conditions for elastic waves. *Geophysics* 1991; **56**(2):231-241.
6. Liao ZP, Wong HL. A transmitting boundary for the numerical simulation of elastic wave propagation. *Soil Dynamics and Earthquake Engineering* 1984; **3**(4):174-183.
7. Cerjan C, Kosloff D, Kosloff R, Reshef M. A nonreflecting boundary-condition for discrete acoustic and elastic wave-equations. *Geophysics* 1985; **50**(4):705-708.
8. Sochaki J, Kubichek R, George J, Fletcher WR, Smithson S. Absorbing boundary conditions and surface waves. *Geophysics* 1987; **52**(1):60-71.
9. Smith WD. A nonreflecting plane boundary for wave propagation problems. *Journal of Computational Physics* 1974; **15**(4):492-503.
10. Yerli HR, Temel B, Kiral E. Transient infinite elements for 2D soil-structure interaction analysis. *Journal of Geotechnical and Geoenvironmental Engineering* 1998; **124**(10):976-988.
11. Kim DK, Yun CB. Time-domain soil-structure interaction analysis in two-dimensional medium based on analytical frequency-dependent infinite elements. *International Journal for Numerical Methods in Engineering* 2000; **47**(7):1241-1261.
12. Manolis GD, Beskos DE. *Boundary Element Methods in Elastodynamics*. Unwin Hyman: London, 1988.
13. Givoli D, Keller JB. Non-reflecting boundary conditions for elastic waves. *Wave Motion* 1990; **12**(3):261-279.

14. Song C, Wolf JP. The scaled boundary finite-element method — alias consistent infinitesimal finite-element cell method — for elastodynamics. *Computer Methods in Applied Mechanics and Engineering* 1997; **147**(3–4):329–355.
15. Israil ASM, Banerjee PK. Advanced time-domain formulation of BEM for two-dimensional transient elastodynamics. *International Journal for Numerical Methods in Engineering* 1990; **29**(7):1421–1440.
16. Grote MJ, Keller JB. Exact nonreflecting boundary condition for elastic waves. *SIAM Journal on Applied Mathematics* 2000; **60**(3):803–819.
17. Wolf JP, Song C. Consistent infinitesimal finite-element cell method: in-plane motion. *Computer Methods in Applied Mechanics and Engineering* 1995; **123**(1–4):355–370.
18. Kawamoto JD. Solution of nonlinear dynamic structural systems by a hybrid frequency–time-domain approach. Research Report R 83-5, Department of Civil Engineering, Massachusetts Institute of Technology, Cambridge, MA, 1983.
19. Seed HB, Idriss IM. Influence of soil conditions on ground motions during earthquakes. *Journal of the Soil Mechanics and Foundations Division, ASCE* 1969; **94**(SM1):99–137.
20. Wolf JP. Consistent lumped-parameter models for unbounded soil: Physical representation. *Earthquake Engineering and Structural Dynamics* 1991; **20**(1):11–32.
21. Feltrin G. Absorbing boundaries for the time-domain analysis of dam-reservoir-foundation systems. IBK Bericht Nr. 232, Institute of Structural Engineering, Swiss Federal Institute of Technology Zürich, Birkhäuser Verlag, Basel, 1997.
22. Ruge P, Trinks C, Witte S. Time-domain analysis of unbounded media using mixed-variable formulations. *Earthquake Engineering and Structural Dynamics* 2001; **30**(6):899–925.
23. Bérenger JP. A perfectly matched layer for the absorption of electromagnetic waves. *Journal of Computational Physics* 1994; **114**(2):185–200.
24. Chew WC, Weedon WH. A 3D perfectly matched medium from modified Maxwell’s equations with stretched coordinates. *Microwave and Optical Technology Letters* 1994; **7**(13):599–604.
25. Qi Q, Geers TL. Evaluation of the perfectly matched layer for computational acoustics. *Journal of Computational Physics* 1998; **139**(1):166–183.
26. Hu FQ. On absorbing boundary conditions for linearized Euler equations by a perfectly matched layer. *Journal of Computational Physics* 1996; **129**(1):201–219.

27. Zeng YQ, He JQ, Liu QH. The application of the perfectly matched layer in numerical modeling of wave propagation in poroelastic media. *Geophysics* 2001; **66**(4):1258–1266.
28. Chew WC, Liu QH. Perfectly matched layers for elastodynamics: A new absorbing boundary condition. *Journal of Computational Acoustics* 1996; **4**(4):341–359.
29. Collino F, Tsogka C. Application of the perfectly matched absorbing layer model to the linear elastodynamic problem in anisotropic heterogeneous media. *Geophysics* 2001; **66**(1):294–307.
30. Basu U, Chopra AK. Perfectly matched layers for time-harmonic elastodynamics of unbounded domains: Theory and finite-element implementation. *Computer Methods in Applied Mechanics and Engineering* 2003; To appear.
31. Graff KF. *Wave Motion in Elastic Solids*. Dover: NY, 1975.
32. Makris N. Causal hysteretic element. *Journal of Engineering Mechanics, ASCE* 1997; **123**(11):1209–1214.
33. Zhao L, Cangellaris AC. A general approach for the development of unsplit-field time-domain implementations of Perfectly Matched Layers for FDTD grid truncation. *IEEE Microwave and Guided Wave Letters* 1996; **6**(5):209–211.
34. Zienkiewicz OC, Taylor RL. *The Finite Element Method* (5th edn). Butterworth-Heinemann, 2000.
35. Newmark NM. A method of computation for structural dynamics. *Journal of the Engineering Mechanics Division, ASCE* 1959; **85**(EM3):67–94.
36. Chopra AK. *Dynamics of Structures: Theory and Applications to Earthquake Engineering* (2nd edn). Prentice-Hall, 2001.
37. Wolf JP, Song C. *Finite-Element Modelling of Unbounded Media*. Wiley: Chichester, England, 1996.
38. De Moerloose J, Stuchly MA. Behaviour of Bérenger’s ABC for evanescent waves. *IEEE Microwave and Guided Wave Letters* 1995; **5**(10):344–346.
39. Bérenger JP. Application of the CFS PML to the absorption of evanescent waves in waveguides. *IEEE Microwave and Wireless Components Letters* 2002; **12**(6):218–220.
40. Luco JE, Westmann RA. Dynamic response of a rigid footing bonded to an elastic half space. *Journal of Applied Mechanics, ASME* 1972; **39**(2):527–534.
41. Teixeira FL, Chew WC. A general approach to extend Bérenger’s absorbing boundary condition to anisotropic and dispersive media. *IEEE Transactions on Antennas and Propagation* 1998; **46**(9):1386–1387.

NOTATION

Roman symbols

a_0	non-dimensional frequency
\mathbf{a}	nodal accelerations
b	half-width of footing
$\mathbf{B}, \tilde{\mathbf{B}}^e, \tilde{\mathbf{B}}^p, \mathbf{B}^\epsilon, \mathbf{B}^\theta$	compatibility matrices;
c_p, c_s	compressional and shear wave velocities
c_{ij}	damping coefficient of nodal dynamic stiffness of layer on rigid base
$\mathbf{c}^e, \tilde{\mathbf{c}}^e, \mathbf{c}, \tilde{\mathbf{c}}$	element-level and global damping matrices
\mathbf{C}, C_{ijkl}	material stiffness tensor
d	depth of layer
\mathbf{d}	nodal displacements
\mathbf{D}	material moduli matrix
$\{\mathbf{e}_i\}$	standard orthonormal basis
$\mathbf{E}, \hat{\mathbf{E}}$	time integral of $\boldsymbol{\varepsilon}, \hat{\boldsymbol{\varepsilon}}$
f_m, f_c, f_k	see Eq. (18)
f_i^e, f_i^p	attenuation functions
$\mathbf{F}^e, \mathbf{F}^p, \tilde{\mathbf{F}}^e, \tilde{\mathbf{F}}^p$	attenuation tensors; Eq. (14)
F_{ij}	flexibility coefficient of rigid strip-footing, with $i, j \in \{V, H, R\}$
H	(in subscript) horizontal DOF of rigid strip-footing
$i = \sqrt{-1}$	unit imaginary number
Im	imaginary part of a complex number
\mathbf{I}	identity matrix
k_s, k_s^*, k_p	wavenumbers for S and P waves
k_{ij}	stiffness coefficient of nodal dynamic stiffness of layer on rigid base
$\mathbf{k}^e, \tilde{\mathbf{k}}^e, \mathbf{k}$	element-level and global stiffness matrices
L_P	depth of PML
\mathbf{m}^e, \mathbf{m}	element-level and global mass matrices
\mathbf{n}	unit normal to a surface
\mathbf{N}, N_I	nodal shape functions
\mathbf{p}, p_i	direction of wave propagation
\mathbf{p}^e	element-level internal force term
\mathbf{q}	direction of particle motion
\mathbf{Q}, Q_{ij}	rotation-of-basis matrix
R	(in subscript) rocking DOF of rigid strip-footing
$ R , R_{pp} , R_{sp} $	amplitude(s) of wave(s) reflected from the PML
Re	real part of a complex number
S_{ij}	component of dynamic stiffness matrix of layer on rigid base
u, \mathbf{u}	displacement(s)

\mathbf{v}	nodal velocities
V	(in subscript) vertical DOF of rigid strip-footing
w, \mathbf{w}	arbitrary weighting function in weak form
x, x_i, \mathbf{x}	coordinate(s)

Greek symbols

δ_{ij}	Kronecker delta
Δ	differential operator
Δt	time-step size
$\varepsilon, \varepsilon_i, \varepsilon_{ij}, \boldsymbol{\varepsilon}, \hat{\boldsymbol{\varepsilon}}$	strain quantities
ζ	damping ratio for visco-elastic medium
θ	angle of incidence of outgoing wave on PML
κ	bulk modulus
λ_i	complex coordinate stretching function
$\tilde{\boldsymbol{\Lambda}}, \boldsymbol{\Lambda}$	stretch tensors
μ	shear modulus
ν	Poisson's ratio
ρ	mass density
$\sigma, \sigma_i, \sigma_{ij}, \boldsymbol{\sigma}, \hat{\boldsymbol{\sigma}}, \tilde{\boldsymbol{\sigma}}$	stress quantities
$\Sigma, \hat{\Sigma}$	time-integral of $\boldsymbol{\sigma}, \hat{\boldsymbol{\sigma}}$
ω	excitation frequency
Ω	entire bounded domain used for computation
Ω^e	element domain
Ω_{BD}	bounded domain
Ω_{PM}	perfectly matched layer